ACCSCIENCE PUBLISHING

International Journal of Bioprinting

RESEARCH ARTICLE

Multi-material bioprinting using a helical mixer for fabricating fibers with controlled composition

Reza Gharraei[1], Donald J. Bergstrom[2], and Xiongbiao Chen[1,2]*

[1]Division of Biomedical Engineering, College of Engineering, University of Saskatchewan, Saskatoon, Saskatchewan, Canada

[2]Department of Mechanical Engineering, College of Engineering, University of Saskatchewan, Saskatoon, Saskatchewan, Canada

(This article belongs to the *Special Issue*: *Bioprinting for Tissue Engineering and Modeling*)

Abstract

Multi-material bioprinting is a promising technique for fabricating complex, heterogeneous constructs with tailored mechanical and biological properties for tissue engineering applications. Recently, the use of a helical static mixer in bioprinting has shown feasibility for producing fibers from multiple biomaterials. However, the underlying mechanisms of transient stream mixing and the control of composition gradients during the printing process remain insufficiently understood. This study investigates biomaterial mixing with the objective of improving the spatial resolution of composition gradients along the longitudinal axis of printed fibers. Computational fluid dynamics (CFD) simulations were utilized to investigate the flow and mixing behavior of precursor streams, and the insights obtained were used to redesign the bioprinting head for improved performance. Rheological studies were performed to characterize the flow behavior of the biomaterials. The results were used, in conjunction with CFD, to examine the mixing performance and to estimate the transition time—defined as the delay between flow rate changes at the inlets and the corresponding change in fiber composition. Our results demonstrate that the redesigned bioprinting head achieved complete mixing of biomaterials and that transition time can be effectively regulated or reduced by preemptively adjusting inlet flow rates. This advancement enhanced the spatial resolution of composition gradients by 17–30%, as confirmed through a case study presented in this article. Additionally, adjustments to the toolpath further improved gradient resolution. Overall, this study elucidates key principles underlying multi-material bioprinting and provides strategies for improving bioprinting head design to achieve finer spatial control of composition gradients.

Keywords: 3D bioprinting; Computational fluid dynamics; Flow behavior; Multi-material bioprinting; Tissue engineering

***Corresponding author:**
Xiongbiao Chen
(xbc719@mail.usask.ca)

Citation: Gharraei R, Bergstrom DJ, Chen X. Multi-material bioprinting using a helical mixer for fabricating fibers with controlled composition. *Int J Bioprint*. 2025;11(5):231-265. doi: 10.36922/IJB025140119

Received: April 2, 2025
1st revised: June 8, 2025
2nd revised: June 27, 2025
Accepted: July 1, 2025
Published Online: July 1, 2025

1. Introduction

Three-dimensional (3D) bioprinting has attracted significant attention for the fabrication of constructs and scaffolds in tissue engineering. This technology allows for the production of constructs with customized internal architectures, mechanical and biological properties, and the incorporation of bioactive agents such as drugs and

growth factors, all aimed at mimicking the structure and composition of native tissues.[1–4] Native tissues are inherently heterogeneous, composed of diverse material and cell types organized into complex architectures that support specific biological functions. Successfully replicating this complexity requires reproducing both the compositional and structural heterogeneity, which in turn demands the integration of multiple biomaterials and various cell types during the bioprinting process.[5–7] Multi-material bioprinting is an emerging technique that facilitates the printing of multiple biomaterials and cell types, as well as the control of compositional gradients within the printed constructs. This approach markedly enhances the capacity to replicate the heterogeneous structure of native tissues.[6,8–11] Various techniques have been adopted to achieve multi-material bioprinting, such as the use of multiple dispensing heads,[12–16] selector valves,[17–19] and/or microfluidic systems.[19,20] One such method involves a multi-material printing head equipped with a microfluidic mixing system, which can extrude a single fiber composed of a controlled gradient of biomaterials along its length. Despite its promise, microfluidic bioprinting faces several limitations. The narrow flow paths inherent to microfluidic channels can generate high shear stresses that may compromise cell viability during extrusion.[4,21,22] As an alternative, mixing strategies involving static mixers—particularly helical static mixers—have gained popularity due to their simple geometry and effective mixing performance.[23,24] Alternating twisted helical elements facilitate stream mixing via chaotic advection, which is the most efficient mechanism for mixing in creeping flows characterized by extremely low Reynolds number, where inertial forces are negligible and mixing is achieved through vortex generation.[25,26]

Although the use of a helical mixer has been demonstrated to be feasible for printing multi-material fibers,[26–29] many aspects remain unexplored, particularly regarding the mixing behavior of multiple flow streams and their influence on bioprinting performance. In a multi-material bioprinting head, precise manipulation of biomaterial flow rates at the inlets is essential for controlling the composition of the outflow stream along the longitudinal axis. This control enables the printing of scaffolds with controlled property gradients that mimic the heterogeneous structure of natural tissues. However, due to the internal volume between the inlets and the outlet of the print head, changes in precursor flow rates at the inlets do not immediately result in corresponding changes in fiber composition at the outlet. This delay is referred to as the transition time (t_t). Notably, the transition time is a dynamic parameter that depends on the internal biomaterial volume of the print head, the initial composition of the flow, and the targeted composition in the printed fiber. Figure 1 illustrates two major challenges encountered during compositional transitions in multi-material bioprinting. During the transition phase, the deposited fiber contains varying fractions of the precursor materials, gradually shifting from the initial to the intended composition (Figure 1A). Therefore, minimizing the transition time is crucial for improving the spatial resolution of property gradients in printed fibers. Furthermore, if the precursor streams are not well mixed during this phase, streaky patterns may emerge in the printed fiber[10,17] (Figure 1B). These streaks can result in weak points along the fiber,

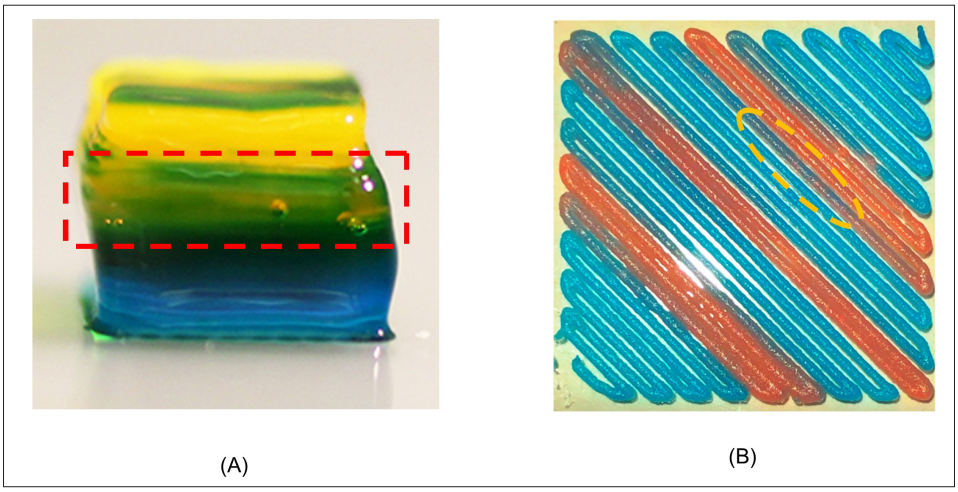

Figure 1. Composition changes in multi-material scaffolds. (A) Transition region with variable composition in a printed multi-material construct. Reprinted with permission from Ref.[10] Copyright © 2016 WILEY-VCH Verlag GmbH & Co. KGaA, Weinheim. (B) Streaky fiber pattern resulting from incomplete mixing during composition change.[17]

especially at locations with abrupt compositional changes, increasing the risk of mechanical failure.

This issue can be addressed by improving the mixing efficiency of the multi-material print head during its transient operation. A precise and comprehensive understanding of the flow and mixing processes enables refinement of inlet flow rate control, thereby improving composition modulation throughout the multi-material bioprinting process. Unfortunately, the dynamics of compositional transition and associated problems (such as the formation of streaky patterns) have not been thoroughly investigated and elucidated in the literature, largely due to the complexity of the system and challenges related to experimental observation. In this context, computational fluid dynamics (CFD) modeling has recently emerged as a powerful and promising approach.[30–32] CFD employs numerical methods to solve the partial differential equations governing fluid flow and mass transport, providing comprehensive insights into phenomena such as velocity distribution, pressure fields, shear stress, and mass fraction evolution. CFD has been extensively used to predict the performance of extrusion-based bioprinting systems, including conventional and coaxial print heads, under varying operational conditions such as different extrusion pressures and printing speeds.[30,33–36] It has also been applied to evaluate the performance of helical mixers, particularly in predicting the striated internal structure of fibers generated by chaotic flows—referred to as chaotic printing.[37,38]

Studies have shown that CFD simulations of biomaterials mixing in multi-material bioprinting heads equipped with helical mixers can elucidate velocity and shear stress distributions in cylindrical and conical nozzle geometries, providing valuable insights for optimizing bioprinting performance.[39] Other studies have reported that CFD can assist in the design optimization of multi-material bioprinting heads.[40] For instance, it was found that increasing the inclination angle of helical mixing elements elevates shear stress, and that these simulated shear stresses correlate with cell viability outcomes from live/dead assays using alginate-based bioinks containing MC3T3-E1 mouse embryonic osteoblasts. It is important to note, however, that the aforementioned studies were performed under steady-state flow conditions, focusing primarily on the impact of print head and mixer geometry on shear stress distribution and mixing performance. These studies did not consider transitional flow conditions, as encountered during compositional changes in multi-material bioprinting. As such, the literature remains limited in its exploration of transient precursor mixing, the dynamics of transition time, and the potential structural and biological issues associated with gradient-based multi-material bioprinting.

This paper presents a study on the multi-material bioprinting process using a helical mixer to print fibers with controlled compositional gradients. CFD was utilized to investigate the flow and mixing behavior of precursor streams within a multi-material bioprinting head, and the CFD simulation results were used to inform the design of a bioprinting head optimized for improved performance. Unlike previous studies,[30,33–39] the present work explicitly considers the effect of biomaterial volume within the bioprinting head and reveals its influence on the transition dynamics during changes in fiber composition.[30,39] The flow behavior of the biomaterials and their mixture at different temperatures was characterized using a parallel plate rheometer. A composition- and temperature-dependent model was developed to represent their rheological behavior accurately. Furthermore, mathematical equations were derived to relate the inlet stream compositions and flow rates to the resulting fiber composition in the multi-material bioprinting process. The designed bioprinting head was evaluated using two distinct biomaterials, and transition times for composition changes in the printed fibers were calculated based on CFD simulation results. In addition to demonstrating the successful operation of the modified print head for producing composition gradients, the CFD simulations revealed that a predictable portion of the transition time can be eliminated by preemptively adjusting the inlet flow rates. This approach significantly enhances the spatial resolution of compositional gradients, demonstrating its value for multi-material bioprinting. Moreover, by linking the apparent viscosity of the biomaterial mixture at the nozzle outlet to the CFD-predicted transition time, this study proposes strategies to further improve the spatial resolution of composition through adjustments in the bioprinting toolpath.

2. Materials and methods

2.1. Multi-material bioprinting head

Figure 2A and B illustrates the flow geometry of the initial design for a multi-material bioprinting head equipped with a helical mixer and two inlets. The overall geometry resembles that of a T-mixer with a circular cross-section, featuring a helical static mixer to enhance mixing efficiency. This configuration is similar to the basic layouts of multi-material heads reported in previous studies, albeit with certain modifications.[26–28] The tapered and chamfered nozzle geometries were adapted from GA27 Luer lock nozzles, as specified in technical data provided by Nordson-EFD (Nordson, United States of America [USA]).[41] The cylindrical T-shaped body of the head, designed to be compatible with Nordson's Luer lock fittings, was modeled using SOLIDWORKS (Dassault Systèmes, France) computer-aided design (CAD) software.

The geometry of the helical mixing elements was based on the Series 190 spiral mixers available from Nordson-EFD (Nordson, USA). As shown in Figure 2C, the helical static mixer consists of alternating clockwise and counterclockwise 180° twisted plates arranged axially. The leading edge of each element is positioned at a right angle to the trailing edge of the preceding one. These elements were mounted onto a 0.9 mm diameter rod for installation inside the print head. The 3D geometries of the T-shaped head body, the helical mixer, and the printing nozzle were assembled in SOLIDWORKS to construct a complete model of the multi-material bioprinting head. The assembly process in SOLIDWORKS was adjusted to match the geometric and dimensional constraints of real-world components.

Once the head geometry was finalized, ANSYS SpaceClaim software (Ansys, USA) was employed to extract the internal fluid domain (flow geometry) by subtracting

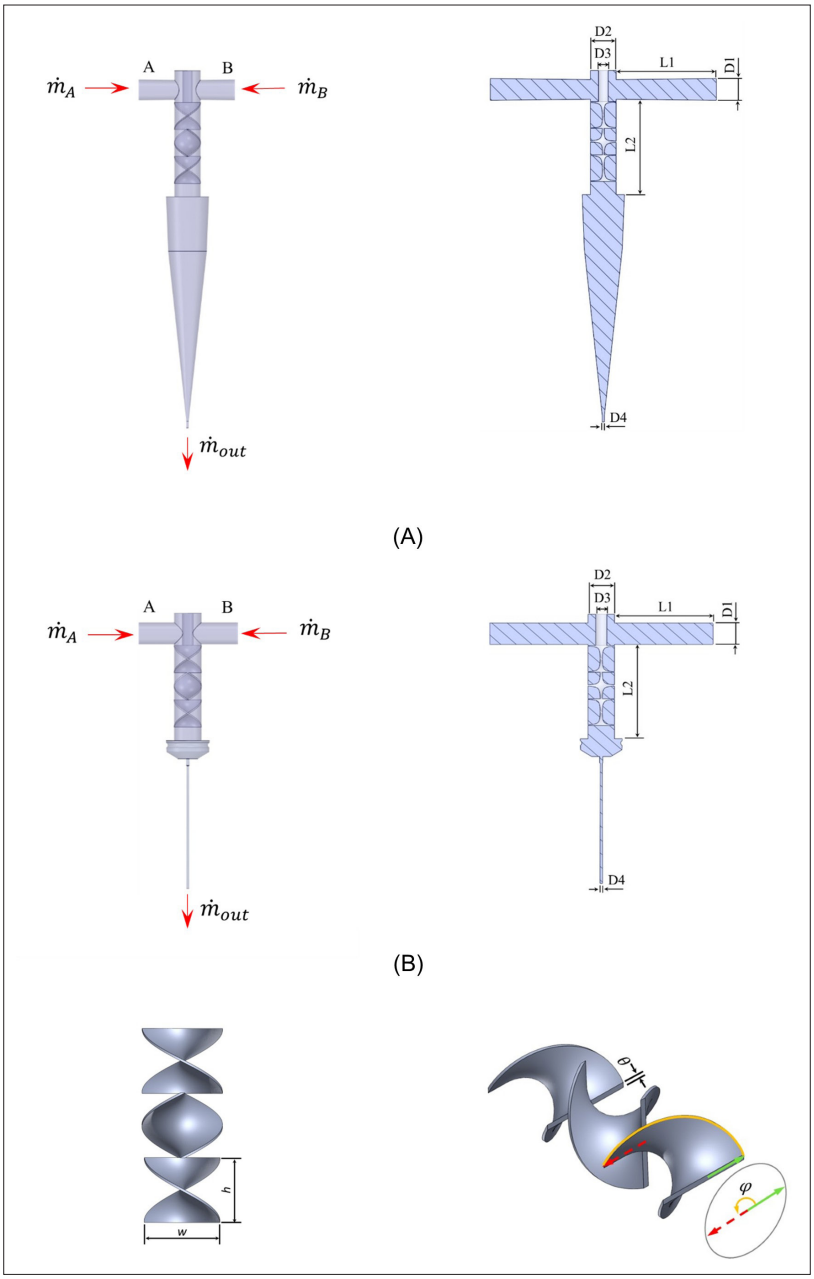

Figure 2. Fluid domain geometry inside the multi-material head with helical mixer connected to (A) a tapered nozzle and (B) a chamfered nozzle. Fluid volume (left); symmetry plane section with dimensions (right). (C) Geometry of the helical mixer (solid body): front view (left) and isometric view (right).

the solid parts from the 3D model. The resulting continuous internal volume was defined as the fluid flow domain for simulation purposes. The dimensional specifications of the fluid domain and the helical mixer elements are presented in Tables 1 and 2, respectively.

The dimensions of the printed head components in this initial design are fully compatible with the helical mixers and Nordson-EFD's Luer lock nozzles. However, these nozzles were not designed for applications involving variable compositions or gradient printing. As a result, they retain a considerable internal volume of fluid, which contributes to delays in transitioning fiber composition during bioprinting.

The composition of the printed fiber corresponds directly to the composition of the outflow stream, which is controlled by the compositions and flow rates of the biomaterials introduced at the two inlets. Assuming that the average velocity of the outflow stream is equal to the printing speed,[42] and that the total flow rate and composition remain constant during a given operational mode, then any increase in flow rate at one inlet must be offset by a corresponding decrease at the other. This reciprocal adjustment alters the composition of the printed fiber while maintaining a constant total flow rate.

On the other hand, the flow inside the bioprinting head is characterized by creeping flow with an extremely low Reynolds number, indicating minimal natural mixing. The alternating twist of the helical mixing elements creates a striated structure within the flow by dividing the stream into two sub-streams, which are then radially redistributed and recombined in an alternating pattern. This process induces chaotic advection, the most efficient mixing mechanism at low Reynolds numbers.[25] Therefore, sufficient space should be allocated within the print head to accommodate a static mixer that enhances biomaterial mixing through chaotic advection. This requirement presents a significant design challenge when developing a multi-material print head intended to control fiber composition with minimal transition time.

For the mixing of two streams using helical mixers, the number of striations in the cross-section increases exponentially, given by[43]:

$$s = 2^n \tag{I}$$

where s is the number of striations and n is the number of mixing elements. The average striation thickness is:

$$\delta = \frac{d_p}{s} \tag{II}$$

where d_p denotes the diameter of the flow passage.[25] This striation effect significantly reduces the mixing length and, consequently, the mixing time.[25] The mixing time can be approximated by:

$$t_{mix} = \frac{d_p^2}{Ds^2} \tag{III}$$

The mixing time becomes comparable to the residence time of the flow within the head, which is given by:

Table 1. G1ometrical characteristics of multi-material heads with various nozzles and helical mixers (all dimensions[a] in millimeter)

Nozzle type	Mixer diameter	D1	D2	D3	D4	L1	L2
Tapered	3.18	2.0	3.18	0.9	0.2	10.0	8.8
	2.36	2.0	2.36	0.9	0.2	10.0	8.8
Chamfered	3.18	2.0	3.18	0.9	0.2	10.0	9.7
	2.36	2.0	2.36	0.9	0.2	10.0	9.7
Conical	2.36	2.0	2.36	0.9	0.2	10.0	7.4
	1.8	1.6	1.8	0.6	0.2	10.0	7.4

[a]Dimensions based on the geometry of nozzles, mixers, and connection of parts in SOLIDWORK assemblies (except for the 1.8 mm conical nozzle that has a customized geometry).

Table 2. Geometrical characteristics of Series 190 spiral mixers from Nordson[41] (all dimensions in millimeter)

Diameter (w)[a]	Element length (h)	Element thickness (θ)	Twist angle (φ)
3.18	2.75	0.62	180°
2.36	2.46	0.4	180°

Note: aAs a customized geometry, 1.8 mm helical mixers have the same geometrical characteristics as the 2.36 mm ones, except for the smaller diameter.

$$t_{res} = \frac{\ell}{u_m} \quad \text{(IV)}$$

where D, ℓ, and u_m denote the diffusion coefficient, flow passage length, and average flow velocity, respectively.

2.2. Dependencies between inlet and outlet flow conditions

During steady-state operation of the multi-material print head, two aqueous streams enter from inlets A and B with mass flow rates $\dot{m}_A$ and $\dot{m}_B$, respectively. The combined stream exits through the nozzle with a total mass flow rate $\dot{m}_{out}$ (see Figure 2). To ensure smooth fiber deposition with a consistent diameter—assumed equal to the nozzle outlet diameter and neglecting swelling effects—the average velocity is taken to match the print head movement speed V during printing[42]:

$$\dot{m}_{out} = \frac{\pi d^2 \rho V}{4} \quad \text{(V)}$$

where ρ is the fluid density. By the principle of mass conservation:

$$\dot{m}_{out} = \dot{m}_A + \dot{m}_B \quad \text{(VI)}$$

Assume the inlet streams consist of aqueous solutions of biomaterials C1 and C2, with mass fractions $Y_{C1,A}$ and $Y_{C2,B}$ at inlets A and B, respectively. The outflow will then contain mass fractions $Y_{C1,out}$ and $Y_{C2,out}$. The concentration ratio of precursors at the outlet, denoted ψ, is defined as:

$$\psi = \frac{Y_{C1,out}}{Y_{C2,out}} \quad \text{(VII)}$$

For a given printing condition, this concentration ratio represents the composition of the printed fiber. To simplify composition control, a reference operation is defined in which the two inlet streams are mixed in a 1:1 ratio:

$$\dot{m}_{A,ref} = \dot{m}_{B,ref} = \frac{\dot{m}_{out}}{2} \quad \text{(VIII)}$$

By applying mass conservation for individual components and through some mathematical operations and rearranging (Appendix A), the following reference relationships are obtained:

$$\psi_{ref} = \frac{Y_{C1,A}}{Y_{C2,B}} \quad \text{(IX)}$$

and:

$$Y_{C1,out,ref} = \frac{\psi_{ref}}{2\left(\psi_{ref}+1\right)}\left(Y_{C1,A} + Y_{C2,B}\right) \quad \text{(X)}$$

$$Y_{C2,out,ref} = \frac{1}{2\left(\psi_{ref}+1\right)}\left(Y_{C1,A} + Y_{C2,B}\right) \quad \text{(XI)}$$

For printability considerations, it is essential to maintain a constant total outflow rate throughout the process. To relate the composition of the outflow stream to the reference case, flow ratios α and β are introduced:

$$\alpha = \frac{Y_{C1,out}}{Y_{C1,out,ref}} = \frac{\dot{m}_{C1,out}}{\dot{m}_{C1,out,ref}} = \frac{\dot{m}_A}{\dot{m}_{A,ref}} \quad \text{(XII)}$$

$$\beta = \frac{Y_{C2,out}}{Y_{C2,out,ref}} = \frac{\dot{m}_{C2,out}}{\dot{m}_{C2,out,ref}} = \frac{\dot{m}_B}{\dot{m}_{B,ref}} \quad \text{(XIII)}$$

These relations describe how the inlet flow rates are scaled relative to their reference values. Notably, α and β satisfy:

$$\alpha + \beta = 2 \quad \text{(XIV)}$$

They can also be expressed in terms of concentration ratios:

$$\alpha = \frac{2\psi}{\psi + \psi_{ref}}, \quad \beta = \frac{2\psi_{ref}}{\psi + \psi_{ref}} \quad \text{(XV)}$$

These relations show that α can be used as a control parameter to adjust the biomaterial flow rates at the inlets to achieve the intended composition ψ at the printed fiber. Appendix A provides detailed steps for deriving the equations listed in this section. **Equations VII, XII, XIV, and XV** are the key governing relationships for controlling printed fiber composition by manipulating the mass flow rates at the two inlets. By adjusting these parameters, the multi-material print head can produce fibers with a controlled longitudinal gradient in composition. Given the known precursor compositions at the inlets ($Y_{C1,A}$, $Y_{C2,B}$)

and the printing speed, the intended ψ can be achieved by appropriately adjusting the α value. The algorithm for this adjustment will be discussed in the following sections.

Any change in the inlet flow rates initiates a transient flow regime, triggered by the application of step-function inputs at both inlets. A new steady-state condition is established after a transition period, which is required for the complete change in the composition of the outflow.

2.3. Preparation of biomaterials

Medium-viscosity sodium alginate salt derived from brown algae (CAS no. 9005-38-3) and medium-viscosity sodium carboxymethylcellulose (CMC) salt (CAS no. 9004-32-4) were procured from Sigma-Aldrich (USA). Aqueous solutions at specified concentrations (mass fractions) were prepared by first blending the dry powders in desired mass ratios, followed by dissolution in Milli-Q water. After preparation, the solutions were allowed to stand undisturbed for 6 h to relieve any residual stresses and to eliminate bubbles that may have formed during the mixing process.

2.4. Rheology

All rheological measurements were performed using a Discovery HR-20 Rheometer (TA Instruments, USA) with 60 mm parallel plates, under controlled temperatures ranging from 10 to 40°C. Samples were gently loaded onto the bottom plate using a spatula, and the upper plate was lowered slowly to prevent disruption of the fluid structure. The samples were then allowed to rest for 10 min prior to testing. Flow curves were obtained by applying shear rates ranging from 0.01 to 1000 s^{-1}.

The apparent viscosity η is defined using a generalized form of the viscosity law, which relates the shear stress tensor ($\overline{\overline{\tau}}$) to the strain rate tensor ($\overline{\overline{\dot{\gamma}}}$) as follows[44]:

$$\overline{\overline{\tau}} = \eta \overline{\overline{\dot{\gamma}}} \quad \text{(XVI)}$$

For a Newtonian fluid, η is the constant dynamic viscosity. However, for non-Newtonian fluids, η varies with the strain rate.

Several time-independent mathematical models describe the flow behavior of non-Newtonian biomaterials by expressing apparent viscosity as a function of shear rate. The model that best fit the steady shear behavior of the tested fluids was selected using TRIOS software (TA Instruments, USA), which analyzes rheological data acquired from the rheometer.

In addition to steady shear tests, oscillatory shear tests were conducted on alginate and CMC aqueous solutions at different temperatures to determine the storage (G′) and loss moduli (G′), thereby characterizing the rheological behavior of the solutions. However, due to the limited ability of current mathematical viscoelastic models to accurately describe the flow behavior of mixtures (as discussed in **Section 3.1**), the rheological investigation primarily focused on steady shear rheology.

Results from steady shear tests on alginate, CMC, and alginate–CMC aqueous solutions—with various mass fractions and tested across multiple temperatures—were used to develop a composition- and temperature-dependent non-Newtonian viscosity model. This model captures how the mixture's flow behavior evolves during mixing inside the print head. The experiments followed a design matrix generated in Minitab (Minitab LLC, USA) for a design of experiments (DOE) at 25°C, covering alginate–CMC mixtures with alginate mass fractions ranging from 0 to 4% and CMC from 0 to 1%. To examine temperature dependency, a second DOE was generated, covering the temperature range of 10–40°C. All tests were performed in triplicate, and concentrations are presented as mass fractions.

To relate the apparent viscosity of alginate–CMC solutions to the mass fraction of the biomaterials, composition-dependent equations were fitted to the parameters of the selected non-Newtonian model. Data analysis was performed using OriginPRO 2021b (OriginLab, USA). Surface equations were fitted using alginate and CMC mass fractions as independent variables and the non-Newtonian model parameters as dependent variables. Temperature dependence was incorporated by fitting Arrhenius-type equations to the temperature-dependent apparent viscosity data for various compositions.

2.5. Governing equations and numerical methods

Assuming incompressible flow, the governing equations for biomaterial flow are expressed as follows[45]:

Continuity equation:

$$\frac{\partial \rho}{\partial t} + \nabla . \rho \vec{U} = 0 \quad \text{(XVII)}$$

Momentum transport equation:

$$\frac{D\left(\rho \vec{U}\right)}{Dt} = -\nabla \mathrm{p} + \nabla . \overline{\overline{\tau}} + \rho \vec{g} \quad \text{(XVIII)}$$

where $\frac{D}{Dt}$ is the material derivative, $\vec{U}$ is the fluid velocity vector, $\vec{g}$ is the gravitational acceleration vector,

and p and ρ denote the pressure and density of the fluid, respectively.

The mixing of biomaterials is modeled by solving the convection–diffusion transport equation for each component, assuming no chemical reactions or phase changes[45]:

$$\frac{D(\rho Y_i)}{Dt} = -\nabla.\vec{J}_i \quad \text{(XIX)}$$

where the diffusion flux is given by:

$$\vec{J}_i = -\rho D_i \nabla Y_i \quad \text{(XX)}$$

Here, Y_i is the mass fraction of i component, and D_i is its diffusion coefficient in the mixture. The diffusion coefficients of alginate and CMC in aqueous solutions at 25°C were taken as 0.78×10^{-9} m^2/s and 0.49×10^{-9} m^2/s, respectively.[46,47]

The governing equations, along with appropriate boundary conditions and flow behavior models, were solved using the finite-volume CFD software ANSYS Fluent 2021-R1 (ANSYS, USA). Polyhedral meshes were generated using ANSYS Fluent Meshing, with local mesh refinement around small geometric features (e.g., the thickness of the helical mixer elements). Mass flow inlet boundary conditions specifying the component mass fractions were applied at the inlets, while a pressure outlet boundary condition with ambient pressure was set at the outlet of the multi-material bioprinting head. Additionally, a no-slip condition with a zero-gradient condition for mass fractions was applied on all solid walls. All simulations employed a pressure-based solver with the SIMPLEC algorithm for pressure–velocity coupling and the QUICK scheme for spatial discretization of the momentum and component transport equations. Grid independence was verified for all cases by examining the axial velocity profile at the outlet boundary.

To calculate the apparent viscosity of alginate, CMC, and their ternary mixtures, user-defined functions (UDFs) were written and interpreted to the Fluent solver. These UDFs calculated the parameters of the composition-dependent viscosity model (at 25°C) and updated the apparent viscosity distribution within the flow domain after each step of the numerical solution.

2.6. Validation

While CFD is a powerful tool for analyzing fluid flow and mixing, it is important to validate the validity of the numerical results by comparing them with experimental data for simplified flow scenarios that share similar physics and geometry with the original problem. Given that the intended multi-material bioprinting process involves fluid flow and mixing through a helical static mixer and a nozzle, validation was performed using both experimental results and empirical correlations related to flow and mixing in helical mixers,[24,48–53] as well as extrusion through a tapered nozzle. Figure B1 (Appendix B) shows the geometry of the fluid domain used to simulate flow and mixing through a helical mixer with a diameter of 3.18 mm. Table 2 provides the geometrical specifications of the helical mixer employed in the CFD simulations. The mixer was positioned 300 mm downstream from the inlet and 200 mm upstream of the outlet of a pipe with the same diameter.

Experimental studies reported in the literature primarily focus on the flow and mixing of Newtonian and power-law non-Newtonian fluids in helical mixers.[24,48–53] The power-law model, one of the simplest non-Newtonian fluid models, describes the relationship between shear stress and shear rate in a simple shear flow as follows[44]:

$$\tau = K\dot{\gamma}^n \quad \text{(XXI)}$$

where K and n are the consistency coefficient and power-law index, respectively. The apparent viscosity is defined as:

$$\eta = K\bar{\dot{\gamma}}^{n-1} \quad \text{(XXII)}$$

where $\bar{\dot{\gamma}}$ denotes the magnitude of the shear rate. This formulation allows the generalized viscosity law (**Equation XVI**) to be applied to power-law fluids.

Table 3 lists the physical and rheological properties of the Newtonian and non-Newtonian fluids considered for validation of flow and mixing in the helical mixers.[48,54] For all cases, mass flow inlet and pressure outlet boundary conditions were applied at the respective boundaries, while all solid walls were treated with a no-slip condition.

Given the role of stress distribution and the striated flow patterns generated by the helical mixer in promoting mixing, validating CFD results against a hydrodynamic parameter such as the friction factor is crucial. The friction factor calculated from the CFD results for both Newtonian and non-Newtonian fluids was compared against empirical correlations from the literature to assess the accuracy of the numerical simulation. For Newtonian fluids, the Reynolds number and Fanning friction factor are calculated as[44]:

$$Re = \frac{\rho d u_m}{\eta} \quad \text{(XXIII)}$$

$$f = \frac{d\Delta P}{2L\rho u_m^{\ 2}} \quad \text{(XXIV)}$$

where u_m is the average velocity, and d and L are the diameter of the pipe (and mixer) and the length over which the pressure loss is measured, respectively. For power-law fluids, most researchers use a generalized form of these definitions for helical mixer flow[48,52]:

$$Re_{gen} = \frac{d^n u_m^{\ 2-n} \rho}{K\varepsilon^{2-n}\left[\left(3n+1\right)/4n\right]^n 8^{n-1}} \quad \text{(XXV)}$$

$$f = \frac{d\Delta P}{2L\rho u_m^{\ 2}}\varepsilon^2 \quad \text{(XXVI)}$$

Here, ε is the void fraction of the static mixer, set to 0.9 based on the mixer geometry.

Several criteria exist to measure mixing homogeneity,[43,55,56] with the mixing index (MI) being the most commonly used parameter for evaluating homogeneity in a flow cross-section. It is calculated as follows[55,56]:

$$MI = 1 - \sqrt{\frac{\sigma_Y^2}{\sigma_{max}^2}} \quad \text{(XXVII)}$$

$$\sigma_Y = \sqrt{\frac{1}{m}\sum_{j=1}^{m}\left(Y_j - \bar{Y}\right)^2} \quad \text{(XXVIII)}$$

where σ_Y denotes the standard deviation of the mass fraction at a cross-section, σ_{max} is the maximum standard deviation when no mixing occurs,[56] Y_j is the mass fraction at point j, $\bar{Y}$ is the mass fraction in a homogeneous mixture, and m is the number of sampling points. A mixture is generally considered homogeneous when MI exceeds 0.95.[24,43] For the mixing of identical fluid streams, mass flow inlets were applied at both entry points, and a pressure outlet boundary condition was assigned at the outlet. All solid walls were considered as no-slip boundaries. The experimental results of Alloca[23] were used to validate numerical results for mixing. The geometry used was the same as in Figure B1 (Appendix B), except for the inclusion of a secondary stream inlet located along the pipe's centerline. The number of mixing elements varied from 8 to 12. The physical properties of the primary and secondary streams were identical to those listed for the Newtonian fluid in Table 3, and the secondary flow rate was 10% of the primary flow rate.

In order to validate the numerical simulation results for predicting the flow of non-Newtonian biomaterials through a nozzle, experimental tests were performed using the GESIM Bioscaffolder (GESIM Bioinstruments and Microfluidics, Germany). Flow rates of 3 and 4% alginate aqueous solutions were measured as they passed through a GA27 tapered nozzle connected to a 10 mL syringe (Nordson-EFD, USA), driven by various upstream pneumatic pressures.

The geometry used in the simulations was generated by extracting the fluid domain geometry from a solid assembly model created in SOLIDWORKS, which combined the geometries of the 10 mL syringe and the GA27 Luer lock tapered nozzle. The CAD models were adapted from files available on the Nordson website (https://www.3dcontentcentral.com/parts/supplier/EFD,-Inc/71022.aspx).[57] The fluid domain was extracted from the solid assembly file using SpaceClaim. Figure 3 illustrates the geometry of the fluid domain used in the numerical simulations of alginate solution flow through the syringe and tapered nozzle. Given the axisymmetric geometry of the fluid domain, only one quarter of the domain—bounded by two symmetry planes—was modeled in the simulations. Boundary conditions included a pressure inlet at the liquid–gas interface inside the syringe, a pressure outlet at the nozzle outlet, no-slip conditions on all solid walls, and symmetry boundary conditions on the symmetry planes.

During the experimental measurements, the flow rate was measured by weighing the amount of fluid

Table 3. Physical and rheological properties of Newtonian and non-Newtonian fluids used in computational fluid dynamics validation[48,54]

Fluid	Density (kg/m³)	Dynamic viscosity (Pa·s)	Consistency coefficient (Pa·sⁿ)	Power-law index
Newtonian fluid	997	0.001	–	–
Non-Newtonian fluid	1000	–	2.44	0.550

dispensed from the nozzle over a specified time interval. As the GESIM Bioscaffolder employs pneumatic pressure to extrude biomaterials, there are inherent delays at the start and end of flow due to the compressibility of the nitrogen gas. To minimize the effect of these delays, the measurement duration was chosen to be sufficiently long, thereby effectively reducing the effect of pressure ramping on the average flow rate. The results were reported as the average of five measurements conducted at a consistent pneumatic driving pressure. After each measurement, the syringe was refilled to minimize the impact of fluid column height reduction. The average height of the liquid column before and after each test was used to determine the volume of biomaterial within the syringe's fluid domain.

2.7. Improving the geometry of the multi-material head based on computational fluid dynamics simulations

The initial geometry of the multi-material head, shown in Figure 2, was designed to be compatible with tapered and chamfered nozzles and helical static mixers, all commercially available from Nordson. The geometric and dimensional constraints for assembling the mixing elements, Luer lock fitting, and nozzles were adapted from Nordson's specifications.[41,57] Two mixing elements with diameters of 2.36 and 3.18 mm were fitted inside the cylindrical body of the multi-material head, which serves as the mixing chamber. The internal diameter of the Luer lock fitting was adjusted to match the diameter of the selected mixer.

CFD simulations were performed to analyze the flow and mixing of two identical 4% alginate streams, designated as alginate-A and alginate-B, within the bioprinting head. Evaluating mixing efficiency using fluids with identical properties is a common approach in numerical and experimental studies to simplify the problem and isolate the effectiveness of the mixing method,[23,53] avoiding complications originating from differences in rheological and diffusive behavior. To further simplify the analysis, both alginate-A and alginate-B were treated as pure fluids, with alginate-A modeled as a passive tracer.[53,58,59] This approach leads to the solution of **Equation XIX**, which governs the mixing of the passive tracer (alginate-A) with alginate-B. The boundary conditions for **Equation XIX** were defined as follows: a mass fraction of 1 at inlet A, 0 at inlet B, and zero-gradient conditions on the solid walls and at the outlet. Solving **Equation XIX** yields the distribution of alginate-A within the flow field, with values ranging from 0 (100% alginate-B) to 1 (100% alginate-A). A value of 1 represents 100% alginate-A (0% alginate-B), and a value of 0 represents 0% alginate-A (100% alginate-B). A value of 0.5 indicates complete mixing, corresponding to a 1:1 mixture. This method provides a clear visualization of the mixing process within the flow field and is specifically

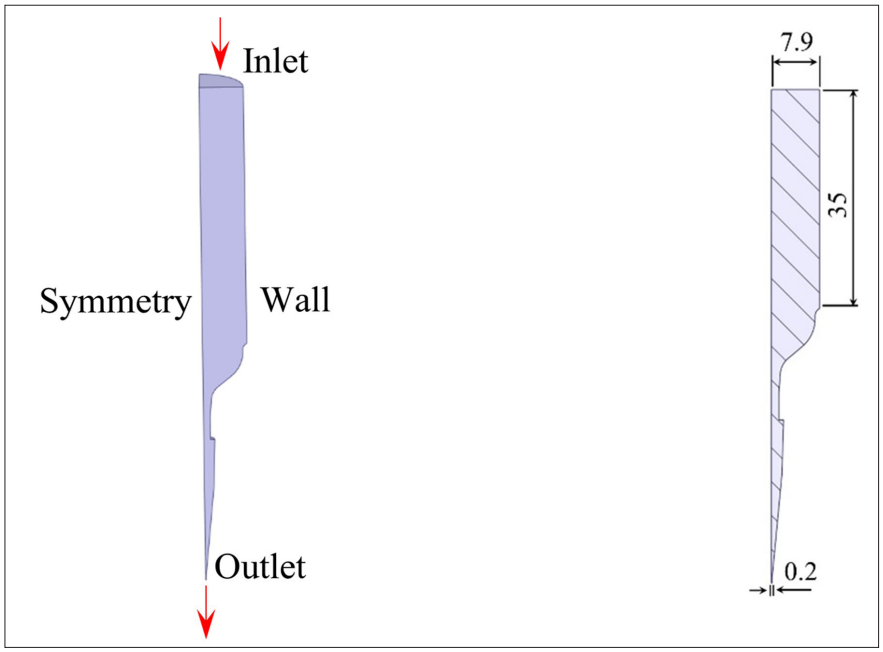

Figure 3. Fluid domain geometry (quarter view) for a GA27 tapered nozzle connected to a 10 mL syringe (left); symmetry plane section with dimensions (right). All dimensions are in millimeter.

applicable to the mixing of two chemically and physically identical solutions.

The results of the simulations were used to examine and refine the initial design of the multi-material head, allowing the identification of optimal geometries and dimensions. After implementing design improvements, the modified geometry was reconstructed in SOLIDWORKS, and the corresponding fluid domain was prepared for further CFD simulations, following the procedure described in **Section 2.1**.

To evaluate the modified design under realistic operating conditions, simulations were performed using a mixture of 4% alginate and 1% CMC aqueous solutions. Alginate–CMC ternary aqueous solutions are widely used in bioprinting and drug delivery applications[60–62] due to their favorable mechanical properties following $CaCl_2$-induced crosslinking. Additionally, CMC enhances cell migration and attachment in fabricated constructs.[62,63] Due to the differing properties of alginate and CMC solutions, **Equation XIX** was solved using the actual mass fraction values of both components. To focus on enhancing the spatial resolution of the composition gradient in multi-material bioprinting, simulations were conducted under the assumption that all printing parameters (e.g., speed, crosslinking, and stage temperature) were properly optimized, ensuring sufficient printability across all intended alginate–CMC compositions. This allowed the study to isolate and examine the flow and mixing dynamics associated with composition transitions, without the confounding effects of material-specific printability constraints. The simulation results also provided crucial insights for designing the flow control system and tool path strategies required for precise, compositional graded printing.

3. Results and discussion

3.1. Flow behavior

Figure 4 presents the results of steady and oscillatory shear rheological tests for 3 and 4% alginate and 1% CMC solutions at various temperatures. The apparent viscosity η is defined by **Equation XVI**. The variation in apparent viscosity shown in Figure 4A and B highlights the shear-thinning behavior of these solutions and the reduction in apparent viscosity with increasing temperature. Meanwhile, G′ and G″ presented in Figure 4C demonstrate the viscoelastic behavior of both alginate and CMC solutions across different temperatures, consistent with findings reported in previous studies.[64,65] However, due to the challenges associated with mathematically modeling viscoelastic behavior, there is currently no model that can accurately describe the rheology of viscoelastic fluids during the mixing process. As a result, time-independent models based on steady shear behavior are typically used in CFD simulations for mixing viscoelastic fluid streams. Accordingly, this study employed time-independent models derived from steady shear test results to simulate the flow and mixing of alginate and CMC aqueous solutions.

Among the various mathematical models evaluated for fitting the steady shear test results, the Cross model[66] was found to provide the best fit, based on goodness-of-fit analysis performed using TRIOS software. For both alginate and CMC solutions, the Cross model achieved a high correlation ($R^2 > 0.99$). The Cross model is a time-independent formulation that describes the apparent viscosity of shear-thinning fluids over a wide range of shear rate[66]:

$$\frac{\eta-\eta_\infty}{\eta_0-\eta_\infty}=\frac{1}{1+k\dot{\gamma}^n} \quad \text{(XXIX)}$$

where k and n are fitting parameters (with $n < 1$), and and η_∞ represent the limiting viscosities at low and high shear rates, respectively. Here, η_0 corresponds to the zero-shear viscosity, typically observed in t η_0 he plateau region at low shear rates, while η_∞, usually a very small value, is treated as a fitting parameter.

Table 4 lists the Cross model fitting parameters for the alginate and CMC solutions at 25°C, along with their densities, which were determined by weighing a known volume of fluid. Previous studies on the rheology of alginate and CMC aqueous solutions have also demonstrated that their flow behavior aligns well with the Cross model.[64,65] Furthermore, steady shear tests conducted on alginate solutions (0.1–4%), CMC solutions (0.1–1%), and alginate–CMC mixtures with various mass fractions confirmed the compatibility of their flow behavior with the Cross model.

Using OriginPRO software, surface fitting was performed to express the Cross model parameters as functions of alginate and CMC mass fractions. The resulting empirical relationships for the composition-dependent Cross model parameters are as follows:

$$\eta_{0,mix}=\Big(2551670.7\ Y_{alg}^{\ 3.34}+\exp\big(407.7\ Y_{CMC}\big)+\Big(256292.29+\exp\big(300.28\ Y_{alg}\big)\Big)\ Y_{alg}Y_{CMC}\Big)\ H_{\eta_0} \quad \text{(XXX)}$$

$$k_{mix}=\Big(21.11Y_{alg}^{\ 1.66}+450941.4\ Y_{CMC}^{\ 2.408}\exp\big(-285.98\ Y_{alg}\big)+2395.91\ Y_{alg}Y_{alg}\Big)H_k \quad \text{(XXXI)}$$

$$n_{mix}=3.74\ Y_{alg}+2025.66\ Y_{CMC}^{\ 2}-25\ Y_{CMC}-254.5\ Y_{alg}\ Y_{CMC}+0.6877 \quad \text{(XXXII)}$$

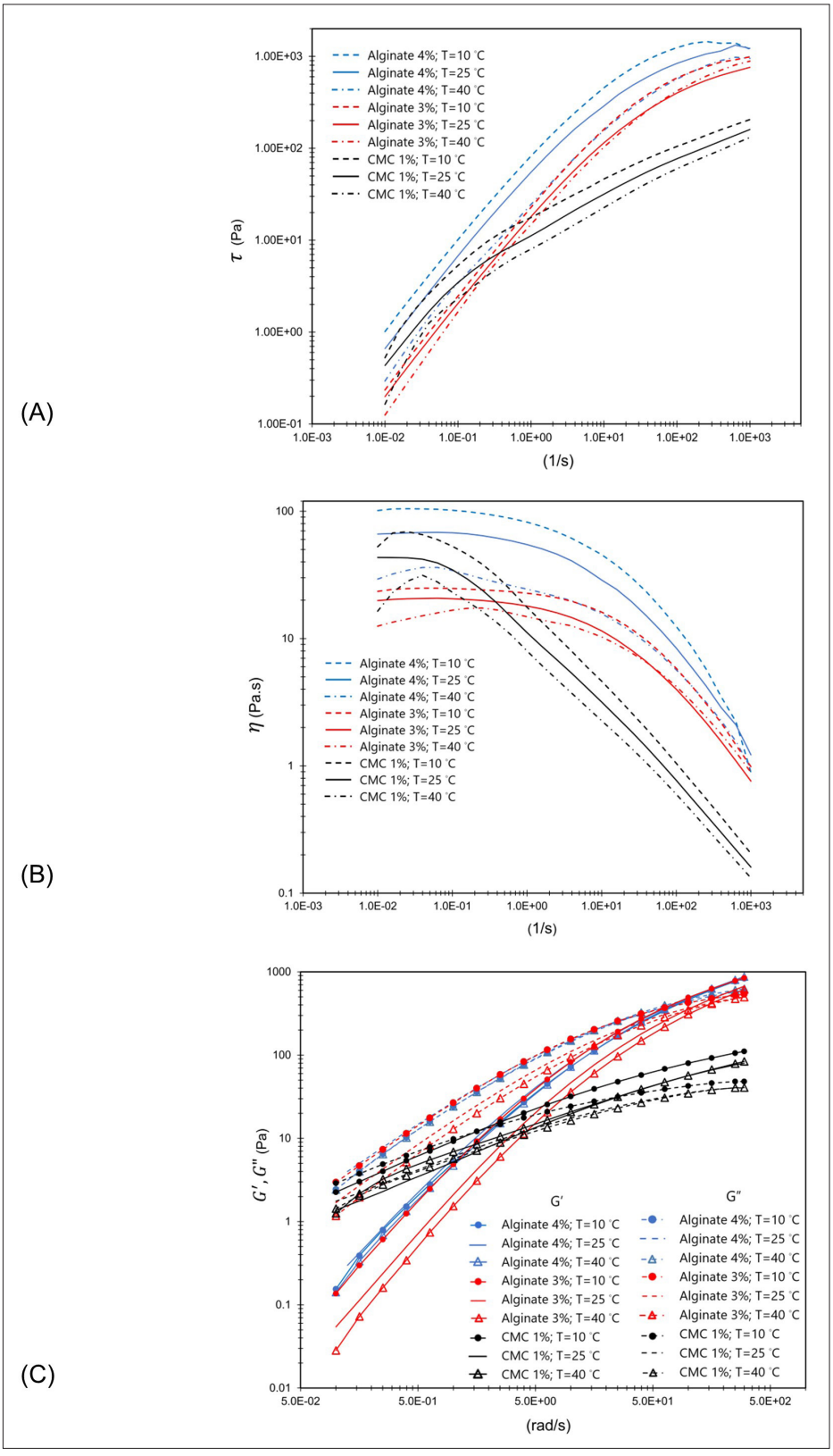

Figure 4. Rheological behavior of biomaterials. (A) Flow behavior, (B) apparent viscosity, and (C) loss (G′) and storage (G″) moduli for 3% alginate, 4% alginate, and carboxymethylcellulose (CMC) 1% aqueous solutions.

where Y_{alg} and Y_{CMC} are the mass fractions of alginate and CMC, respectively, with the valid range $Y_{alg} \leq 0.04$ and $Y_{CMC} \leq 0.01$. The high-shear viscosity ($\eta_{\infty, mix}$) was negligible for all solutions and was omitted from the expressions. The R^2 values for the surface fits were 0.98, 0.97, and 0.93 for $\eta_{0,mix}$, K_{mix}, *and* n_{mix} respectively, indicating excellent agreement with the experimental data.

H_{η_0} and H_k in **Equations XXX and XXXI** are temperature correction functions used to adjust the values of η_0 and k for temperatures other than 25°C. Surface fitting of steady shear test results for alginate–CMC aqueous solutions across a temperature range of 10–40°C resulted in the following Arrhenius-type viscosity correction functions[67,68]:

$$H_{\eta_0} = \exp\left[\frac{E_{\eta_0}}{\mathcal{R}}\left(\frac{1}{T} - \frac{1}{298.15}\right)\right] \quad \text{(XXXIII)}$$

$$H_k = \exp\left[\frac{E_k}{\mathcal{R}}\left(\frac{1}{T} - \frac{1}{298.15}\right)\right] \quad \text{(XXXIV)}$$

where $\mathcal{R} = 8.314$ J/mol·K is the universal gas constant, T is the absolute temperature in Kelvin (K), and E_{η_0} and E_k E_k are the activation energies (in J/mol), both dependent on composition:

$$E_{\eta_0} = \frac{-29590 Y_{alg} + 18205\ Y_{CMC} - 34343 Y_{alg}\ Y_{CMC}}{1 - 2.951 Y_{alg} - 317.70\ Y_{CMC}} \quad \text{(XXXV)}$$

$$E_k = \frac{-307790 Y_{alg} + 170810\ Y_{CMC} - 579870 Y_{alg}\ Y_{CMC}}{1 - 188.83 Y_{alg} + 180.80\ Y_{CMC}} \quad \text{(XXXVI)}$$

3.2. Valuation of numerical results

Figure 5 presents the validation of the numerical simulations for flow through the helical mixer. This figure compares the numerically predicted friction factor f with values calculated from various empirical correlations available in the literature.[24,48–52] Figure 5A and B shows that the numerical results for the Newtonian fluids are in good agreement with the correlations proposed by Cybulski and Werner[49] and Shah and Kale.[48] For non-Newtonian fluid flow, the predicted friction factor closely matches the data reported by Xu et al.[52]

Figure 5C compares the simulation results with experimental data from Alloca[23] for the mixing of two fluid streams through helical mixers with varying numbers of elements, denoted by different L/d values (the ratio of the total mixer length L to the diameter d). This comparison demonstrates strong agreement between the numerical results and experimental data of Alloca.[23] Since no experimental studies have been reported on the flow and mixing of non-Newtonian Cross fluids in helical mixers, validation was carried out using results from experimental studies on Newtonian and power-law non-Newtonian fluids. The Cross model transitions to the Newtonian model as $k \to 0$, and behaves like a power-law fluid when $\eta_\infty \ll \eta \ll \eta_0$,[44,66] which covers a wide range of shear rates typically encountered in helical mixers. Consequently, validation of CFD simulations using existing data on Newtonian and power-law fluids provides an insightful assessment of the reliability of the CFD results for Cross fluids.

Figure 6 compares the numerically predicted flow rates of 3 and 4% alginate solutions through a syringe and nozzle under various upstream pneumatic pressures. Error bars represent uncertainties in flow rate measurements, calculated using the Moffat method.[69] The GESIM Bioscaffolder utilizes pressure regulators with an accuracy of 0.6% of full scale or better, within a pressure range of 0–900 kPa. Its solenoid valves also feature a response time of 25 ms or less. The agreement between experimental and simulation results confirms the accuracy of the numerical model in predicting the flow of a Cross fluid through a nozzle.

Given the demonstrated accuracy of the numerical simulations in predicting flow and mixing in both helical mixers and nozzles, it can be concluded that the CFD approach is reliable for analyzing the flow and mixing of biomaterials within a multi-material bioprinting head equipped with a helical mixer.

Table 4. Density and cross model fitting parameters for alginate and carboxymethylcellulose (CMC) aqueous solutions at T = 25°C

Fluid	ρ (kg/m³)	η_0 (Pa·s)	η_∞ (Pa·s)	k (s)	n
Alginate 3%	998.3	20.52	9.18E-6	0.067	0.770
Alginate 4%	998.7	55.23	4.62E-15	0.095	0.85
CMC 1%	1000	54.8	1.95E-17	6.6	0.66

3.3. Improving the multi-material head geometry based on computational fluid dynamics simulation results

As discussed above, an improved design of the multi-material head should ensure not only high MI but also low shear stress levels and reduced internal volume—factors critical for maintaining cell viability and achieving high spatial resolution in controlled composition gradient multi-material bioprinting. To evaluate performance, the mixing of two 4% alginate solutions was considered as a test case for examining the performance of multi-material heads with different geometric parameters. Figure 7 demonstrates the impact of the number of mixing elements (N) on the MI at the outlet of the multi-material head, for the flow and mixing of two 4% alginate streams (alginate-A and alginate-B). The inlet flow rates were equal, and the average outlet velocity was set to 10 mm/s, consistent with the printing speed. All MI values in Figure 7 exceed 0.95, suggesting that as few as two mixing elements are sufficient to mix two 4% alginate streams within a multi-material head equipped with a chamfered or tapered nozzle. However, as shown in Figure 8, the distribution of the mass fraction indicates that mixing is not complete after the second element; instead, the mixing process continues as the fluid flows through the nozzle.

Table 5 compares the estimated mixing time and residence time for the mixing of 4% alginate solutions using two and three 2.36 mm mixing elements. The results indicate that with two elements, the required mixing time exceeds the residence time for flow through the mixing elements. This suggests that the fluid streams are not thoroughly mixed immediately after the second element, and the remaining mixing is completed inside the nozzle, as shown in Figure 8. According to **Equation III**, the flow through the nozzle needle accelerates mixing due to its extremely small diameter, which enhances the breakdown of striations. When three elements are used, the mixing time closely matches the residence time, resulting in well-mixed streams by the trailing edge of the third element.

Comparing the MI values for 3.18 and 2.36 mm mixing elements in Figure 7 shows that the 2.36 mm elements yield better mixing performance, primarily due to the thinner striations they generate.[28] In addition, the 2.36 mm elements require a smaller internal volume within the head. The maximum shear stress for configurations with three mixing elements of either size, combined with a tapered nozzle, remains nearly constant at 1.45 kPa. However, when a chamfered nozzle is used, this value increases to 2.9 kPa for both mixer sizes. Given that the 2.36 mm elements provide superior mixing and produce similar maximum shear stress levels compared to the 3.18 mm elements, they are the preferred choice for the modified design. Chamfered nozzles, due to their small diameter and high length-to-diameter ratio, facilitate efficient mixing of extremely thin striations and offer a smaller internal volume (as illustrated in Figure 2). However, they also generate significantly higher shear stress than tapered nozzles. As a result, chamfered nozzles were not selected for the improved design of the multi-material head due to potential negative effects on cell viability.

Despite their popularity, tapered nozzles are not ideal for controlled-gradient multi-material bioprinting because they retain a relatively large internal volume, which increases the response time of the head to changes in inlet flow rates. To strike a balance between the small internal volume and high shear stress of chamfered nozzles and the larger internal volume and lower shear stress of tapered nozzles, a simple conical nozzle geometry was considered for the improved multi-material head. Figure 9 illustrates the fluid domain geometry of the multi-material head equipped with a threaded conical nozzle. The nozzle dimensions are provided in Table 1. Unlike tapered nozzles, which have a profile with two distinct cone angles, the conical nozzle consists of a single cone connected to a needle. In contrast to the Luer lock connection used in the initial design, the threaded connection offers greater flexibility in sizing the head.

Due to the space required for Luer lock fittings and the internal geometry of the bioprinting nozzles, the L2 length (as shown in Figure 2) cannot be reduced below 8.8 mm for tapered nozzles or 9.7 mm for chamfered nozzles. This means that even with a single mixing element, the L2 length remains unchanged. In contrast, a customized conical nozzle with a threaded connection does not require additional fitting length, allowing the L2 length in Figure 9 to be equal to the length of the helical mixer installed within the head. While the modified design employs custom components with fewer limitations on size and fittings, its overall geometry and dimensions remain within the range of high-precision nozzles and fittings commercially produced by GESIM and Nordson.

Figure 10 displays the shear stress distribution on the symmetry plane for three different head geometries equipped with tapered, chamfered, and conical nozzles. The results indicate that the maximum shear stress within the helical mixer is less than 5% of the peak value observed at the contraction region of the printing nozzle. This confirms that the mixing elements do not significantly contribute to the maximum shear stress, and that the nozzle shape

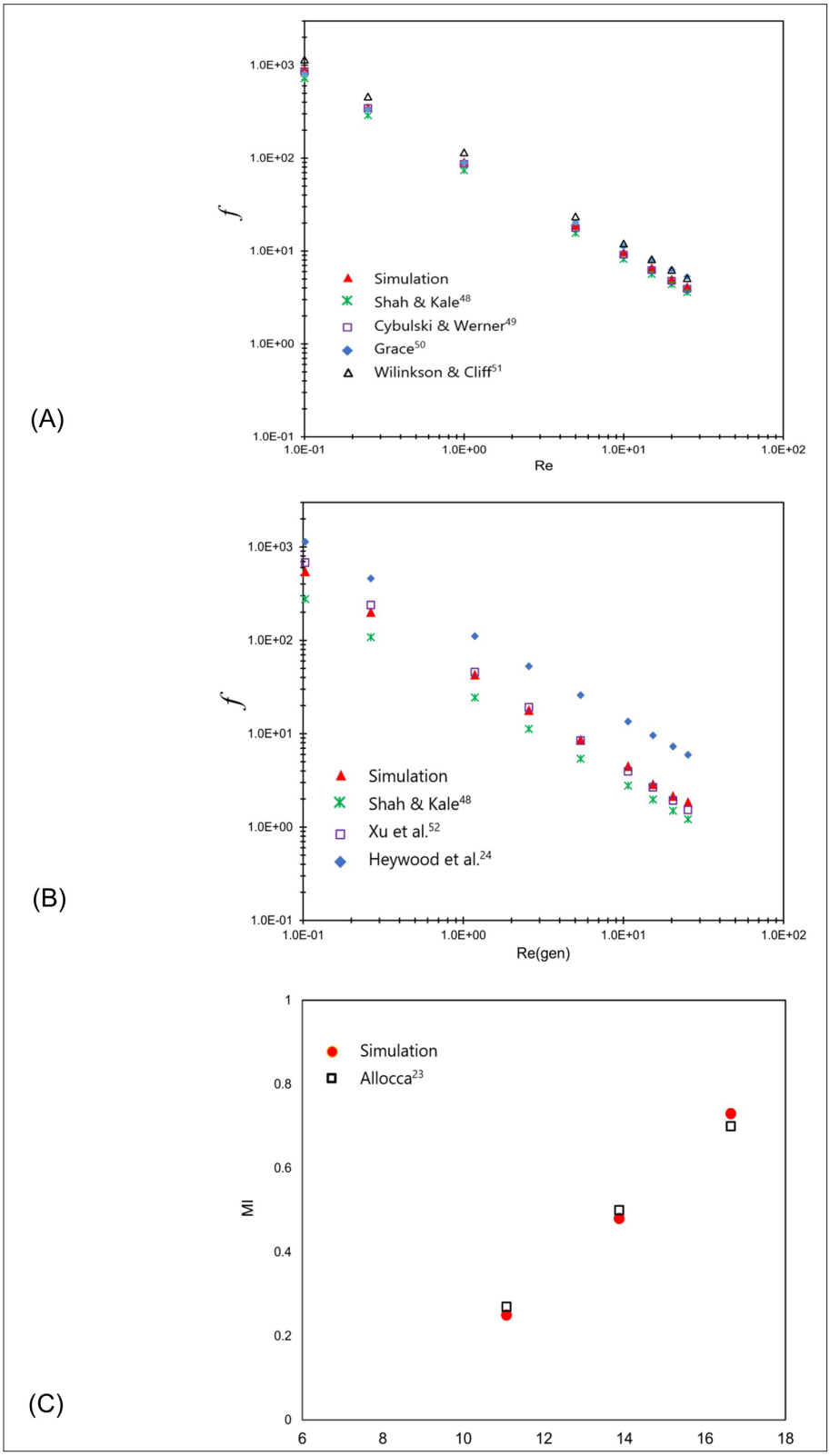

Figure 5. Validation of computational fluid dynamics (CFD) results: Comparison of friction factor predicted by numerical simulations and empirical correlations for (A) Newtonian fluid, (B) for non-Newtonian fluid, and (C) comparison of the mixing index predicted by CFD with the experimental results of Alloca.[23]

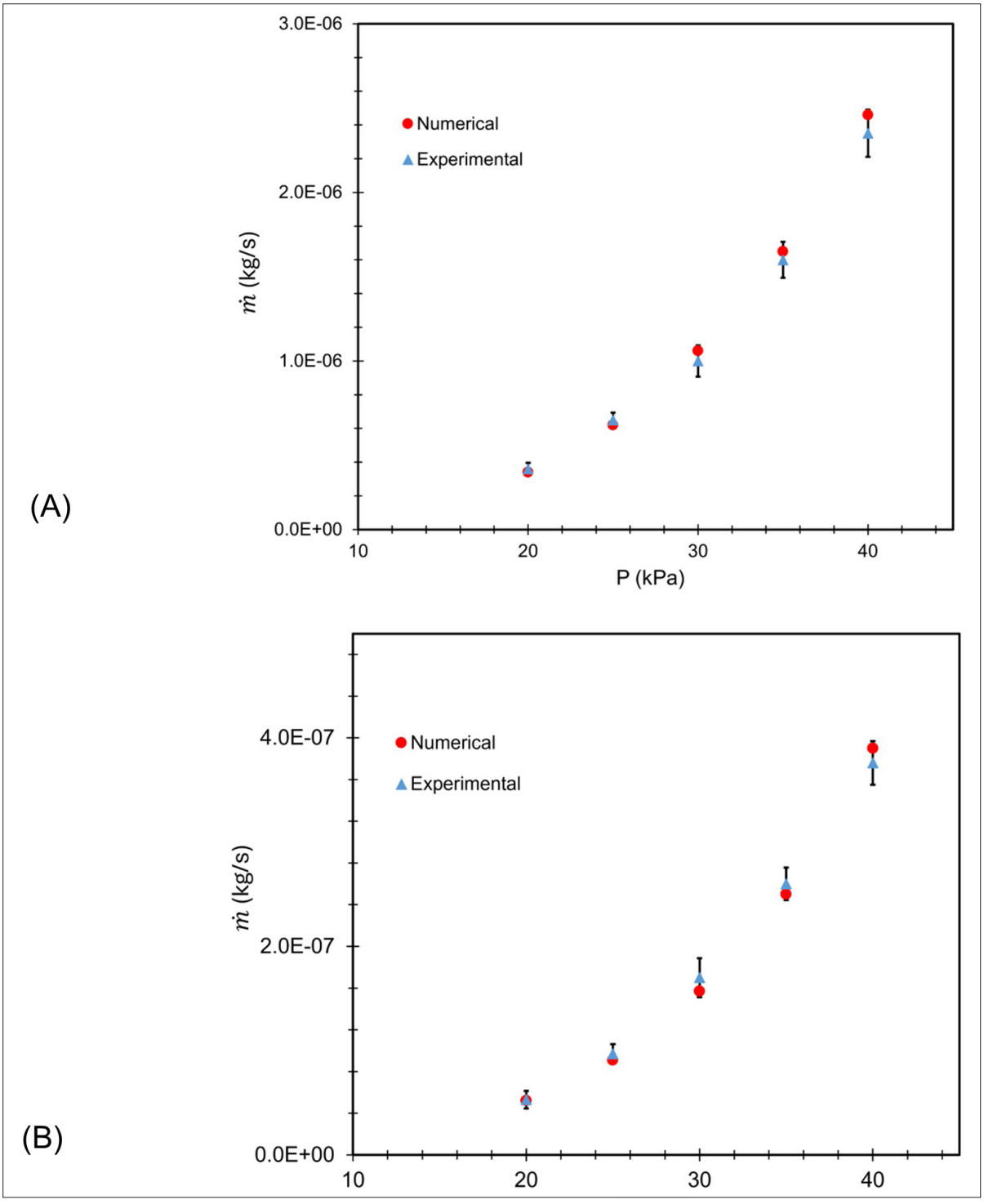

Figure 6. Validation of computational fluid dynamics (CFD) results: Comparison of flow rate predicted by CFD and experimental measurements for the flow of (A) 3% alginate and (B) 4% alginate solutions driven by various upstream pressures.

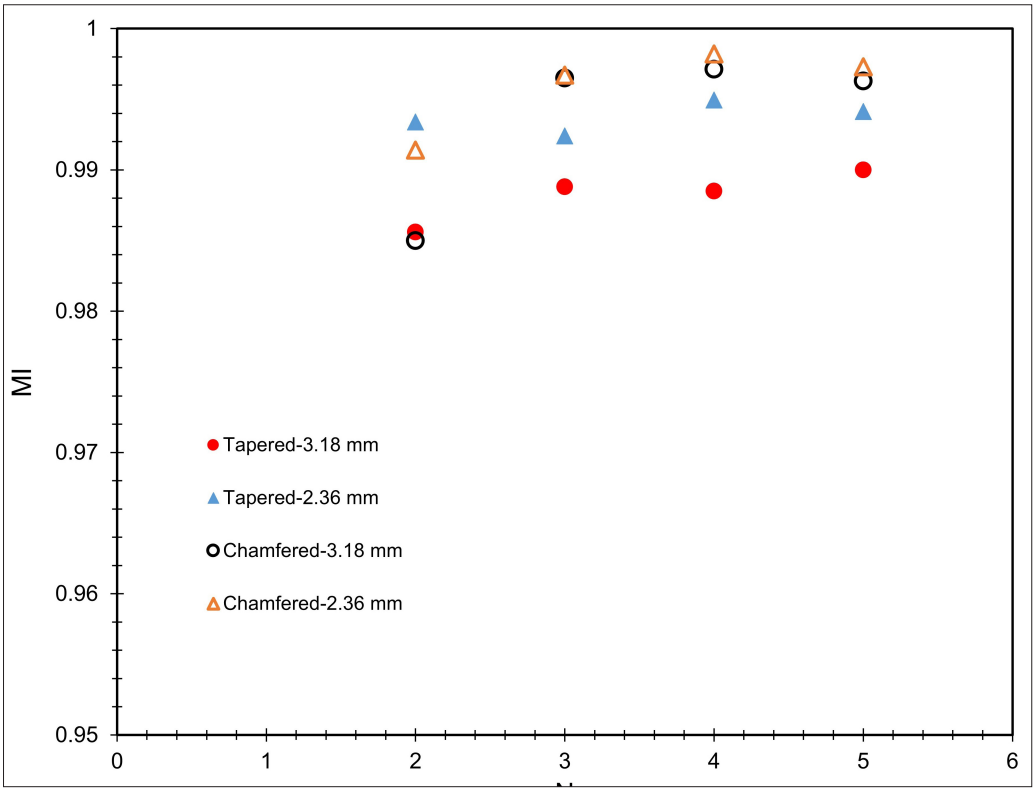

Figure 7. Variation of mixing index (MI) with the number of mixing elements for designs with tapered and chamfered nozzles of different diameters.

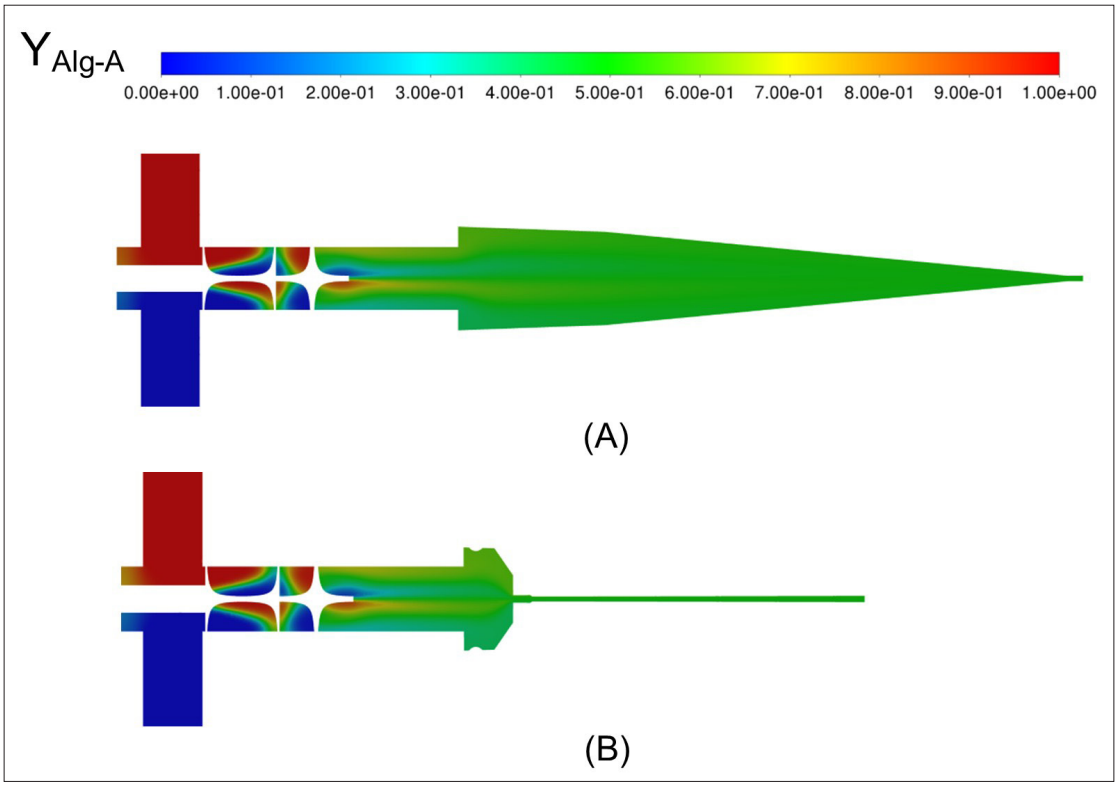

Figure 8. Distribution of alginate-A inside the heads with (A) tapered and (B) chamfered nozzles. Contours are shown on the middle plane of the geometry.

Table 5. Estimated mixing and residence times for 4% alginate solutions through helical mixers (based on Section 2.1)

Number of elements	t_{mix} (s)	t_{res} (s)
2	446.3	68.5
3	111.6	102.8

primarily determines the level of process-induced forces that may affect cell viability during bioprinting.

The distribution of alginate-A inside the multi-material heads, shown in Figure 11, supports the estimations made in Table 3. It demonstrates that the mixing process is almost complete immediately after the third mixing element, with no additional length inside the nozzle required to achieve homogeneity. In other words, with three mixing elements, the influence of nozzle geometry on mixing is minimal. However, the nozzle geometry still affects both the maximum shear stress and the internal volume of the head. As a custom geometry, the conical nozzle is not subject to the size limitations of standard Luer tapered and chamfered nozzles and can be fabricated in arbitrary dimensions. Nevertheless, to avoid excessively narrow flow passages—which would compromise the meso-scale advantage of the multi-material head over micro-scale systems—conical nozzles with outlet diameters of 2.36 and 1.8 mm were selected as candidates for the modified geometry.

Figure 12A compares the MI values for combinations of three mixing elements with 2.36 and 1.8 mm conical nozzles, each with various length-to-diameter ratios ($\frac{l}{d}$). The results show that all tested length-to-diameter ratios yield a homogeneous mixture at the outlet. Once complete mixing is achieved by the three helical elements, the conical nozzle geometry has little effect on the MI. Therefore, MI alone is insufficient for determining the optimal length-to-diameter ratio of the conical nozzle.

Figure 12B and C compares the internal volume ($\mathbb{V}_{head}$) and the maximum shear stress for different nozzle configurations, respectively. Figure 12B shows that changes in the length-to-diameter ratio have only a minor impact on the internal volume. In contrast, Figure 12C shows that the maximum shear stress decreases significantly for $\frac{l}{d} \leq 1.5$, and then levels off for both sizes of mixing elements. Based on the insights from Figure 12A–C, it can be concluded that a head equipped with three 1.8 mm mixing elements and a conical nozzle with $\frac{l}{d} = 1.5$ effectively mixes two 4% alginate streams while maintaining relatively small internal volume and a maximum shear stress comparable to that of a tapered nozzle—currently considered the most favorable option for preserving cell viability. Accordingly, this configuration was chosen as the optimized head geometry for printing biomaterials with properties similar to 4% alginate.

Various criteria have been proposed in the literature[22,70,71] to predict the effect of process-induced forces on cell viability. While cell viability depends on multiple factors, examining the shear stress distribution during the flow of 4% alginate—which is highly viscous and less ideal for cell-laden bioprinting—can help guarantee that shear stress remains within a tolerable range for lower-viscosity biomaterials, such as 2.5 or 3% alginate solutions, which are more suitable for encapsulating cells. The maximum shear stress values shown in Figure 12C are significantly lower than the critical thresholds reported in the literature for potential cell damage, such as for Rat L929 or RAMEC cell lines.[22,70] Therefore, the improved multi-material head geometry is expected to support good cell viability during extrusion. Nevertheless, cell viability is influenced by several factors, such as stress magnitude and duration, cell type, and the physical properties of the biomaterial, and must be evaluated experimentally.[22,70,71] Accordingly, laboratory-based investigations are necessary to draw reliable conclusions about cell viability during and after multi-material extrusion.

While the improvements to the multi-material head were based on numerical simulations involving the mixing of two 4% alginate streams, experimental evaluation of its performance in bioprinting other materials is necessary to assess its broader applicability and limitations. As a case study, multi-material bioprinting using alginate and CMC solutions was conducted to evaluate the performance of the modified head in controlled composition gradient printing.

3.4. Multi-material bioprinting of alginate and carboxymethylcellulose solutions

Mixing 4% alginate and 1% CMC solutions at different ratios was considered a practical case to examine the performance of the modified multi-material head for on-the-fly mixing in controlled-gradient bioprinting. The fiber composition at the outlet is controlled by manipulating the inlet flow rates of the biomaterials, which determine the precursor mixing ratio. This manipulation is achieved by adjusting the α value, which defines the mass flow rates at the inlets according to **Equations XV, XIV, XIII, and XII**. For the mixing of 4% alginate and 1% CMC solutions, the reference parameters are:

$$\psi_{ref} = 4,\ \alpha_{ref} = 1,\ \beta_{ref} = 1 \qquad \text{(XXXVII)}$$

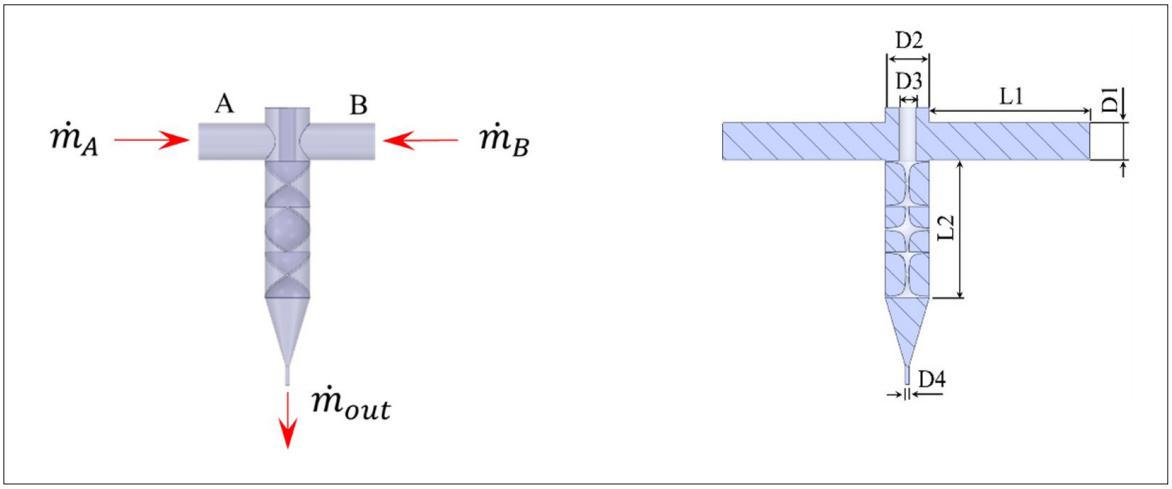

Figure 9. Fluid domain geometry inside the multi-material head with helical mixer connected to a conical nozzle. Fluid domain (left); symmetry plane section with dimensions (right).

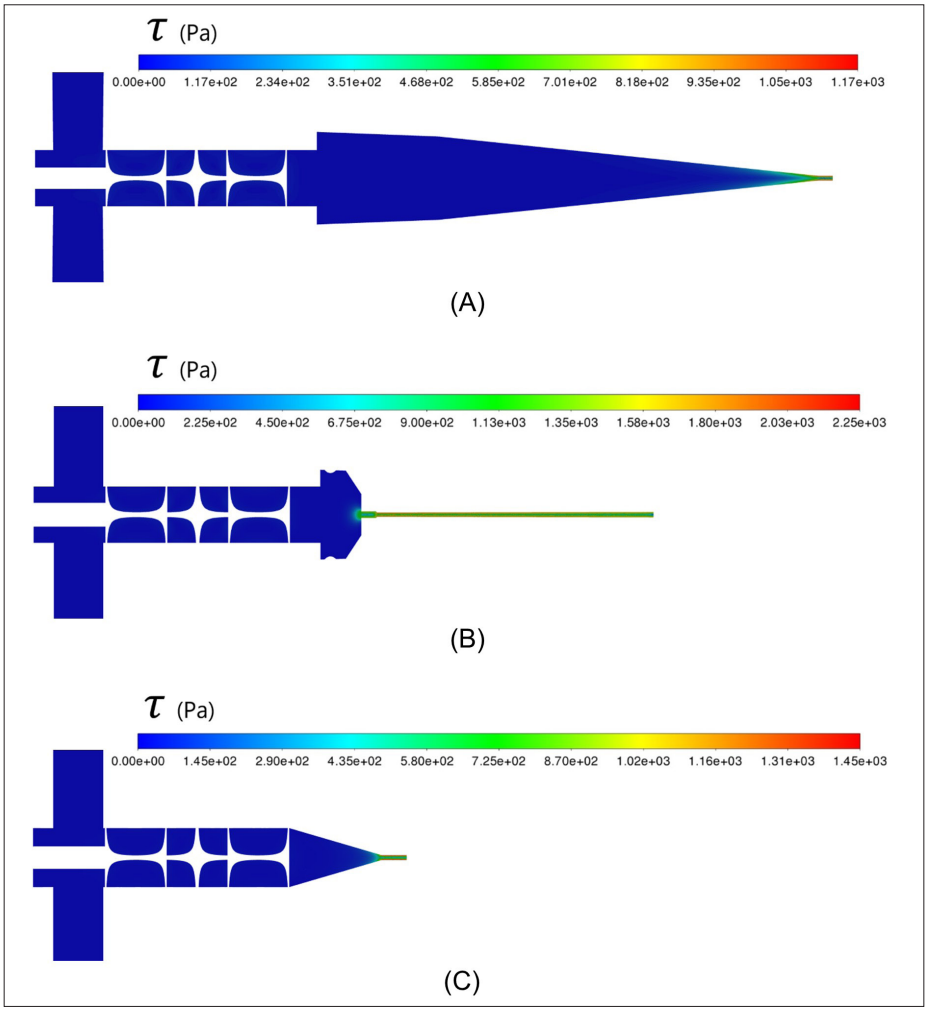

Figure 10. Shear stress distribution for (A) tapered, (B) chamfered, and (C) conical nozzles with d = 2.36 mm. Contours shown on the symmetry plane.

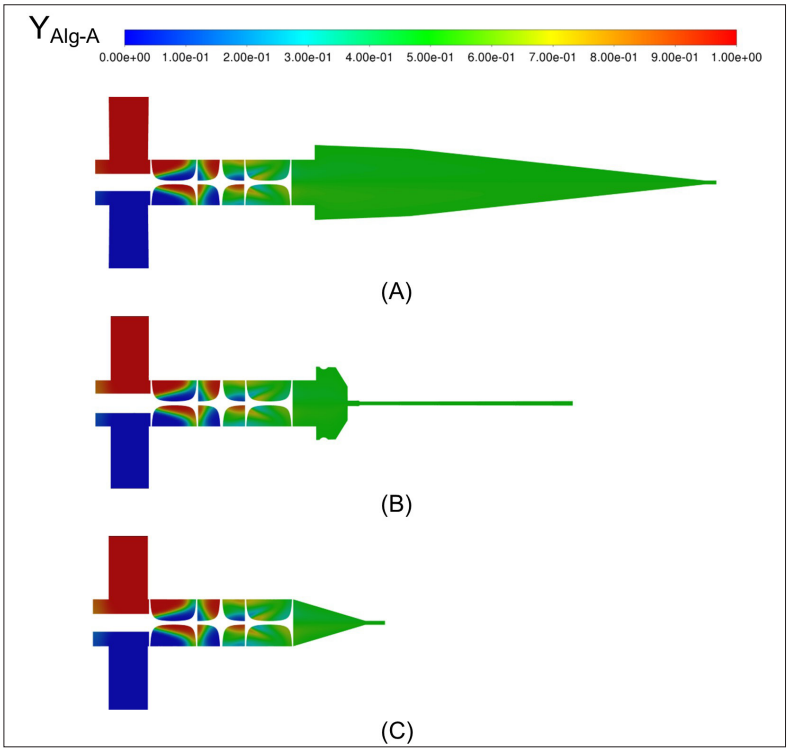

Figure 11. Distribution of alginate-A mass fraction inside the heads with (A) tapered, (B) chamfered, and (C) conical nozzles. Contours shown on the symmetry plane.

Figure 13 illustrates the distribution of alginate and CMC mass fractions inside the head for three different mixing scenarios, each with a distinct α value. The figure qualitatively demonstrates the capability of a multi-material head equipped with helical mixers to combine two biomaterials with different flow rates. Figure 14 provides a more quantitative assessment by comparing MI values across various α values and printing speeds. The results confirm the head's ability to achieve adequate mixing of 4% alginate and 1% CMC solutions over a wide range of ratios, even at a relatively high printing speed of 10 mm/s, which is significant for multi-material bioprinting.[26,72] As expected, slower printing speeds result in lower total flow rates and longer residence times, which facilitate mixing. Therefore, reducing the printing speed to 5 mm/s improves mixing for all tested conditions. Figure 14 also shows improved mixing performance for $\alpha > 1$, representing compositions with higher alginate content. This observation is consistent with previous findings by Jaffer and Wood[73] and Regner et al.,[74] who studied the mixing of Newtonian fluids with varying viscosities using helical mixers and Lightnin Series 45 mixers. While these mixers differ slightly in geometry, their functionality is comparable to that of helical mixers.

One particularly interesting operational mode for a multi-material bioprinting head is the ability to generate controlled composition gradients within a scaffold—essential for creating zonal heterogeneity. As previously discussed, the key factor in controlled composition gradient printing is the transition time required to fully shift from one composition to another at the outlet.

To evaluate this, numerical simulations of unsteady mixing and extrusion were conducted for various composition transitions relative to the reference case (i.e., various α values). Figure 15 illustrates the temporal variation of the normalized concentration ratio, $\frac{\psi}{\psi_{ref}}$, for transitions from $\alpha = 1$ to other values at printing speeds of 10 and 5 mm/s. Time is normalized by the sweep time (t_s), defined as the time to displace the internal volume of the head with the total flow rate (or outlet flow rate):

$$t_s = \frac{\mathbb{V}_{head}}{Q_{out}} \quad \text{(XXXVIII)}$$

Surprisingly, despite the differences in precursor velocities and mixture viscosities, the first deviation from the initial composition consistently occurs at the same interval (t_0), approximately 20–25% of the sweep

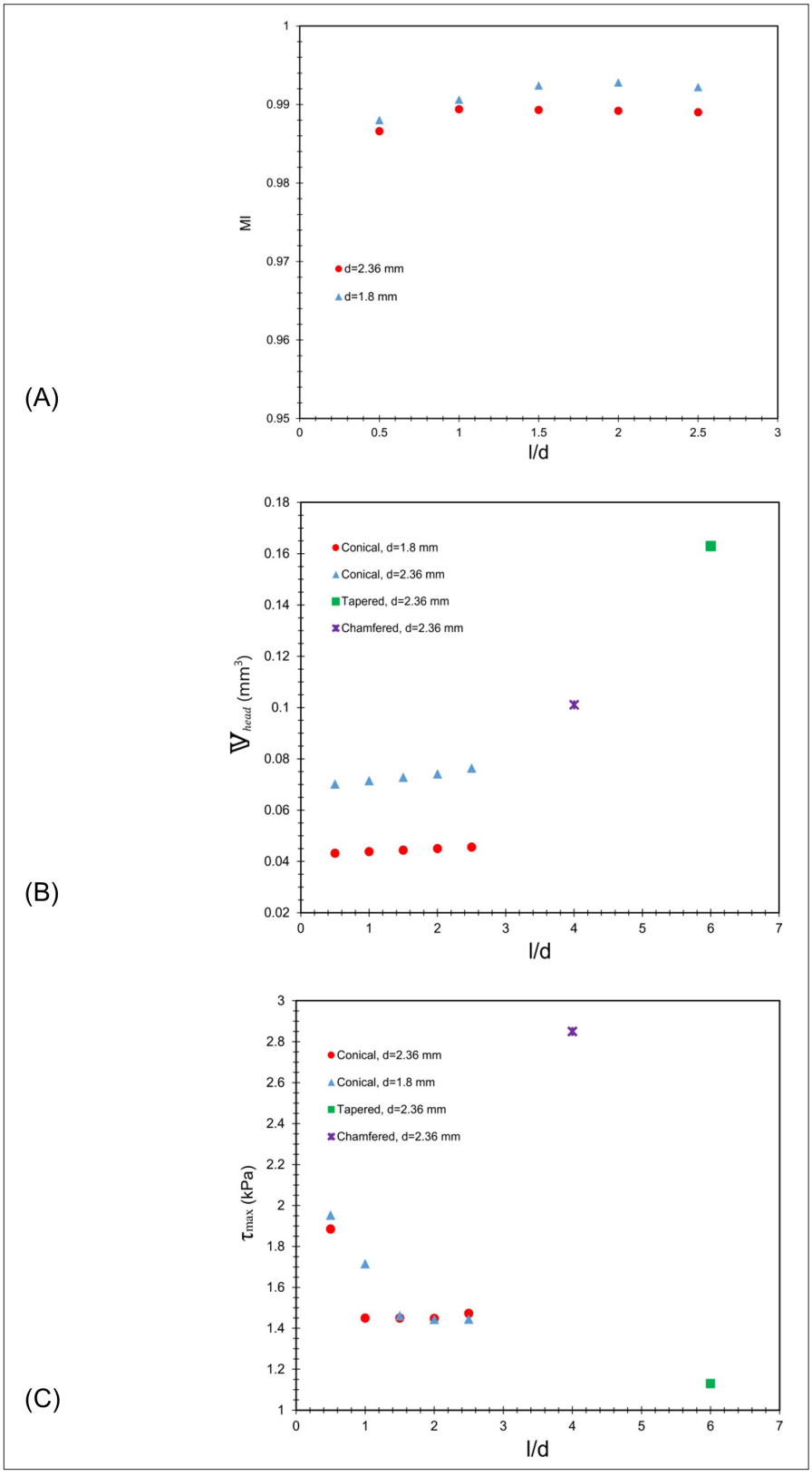

Figure 12. Effect of conical nozzle length-to-diameter ratio (l/d) on key parameters affecting performance in multi-material bioprinting with composition gradients. (A) Mixing index (MI), (B) internal volume, and (C) maximum shear stress.

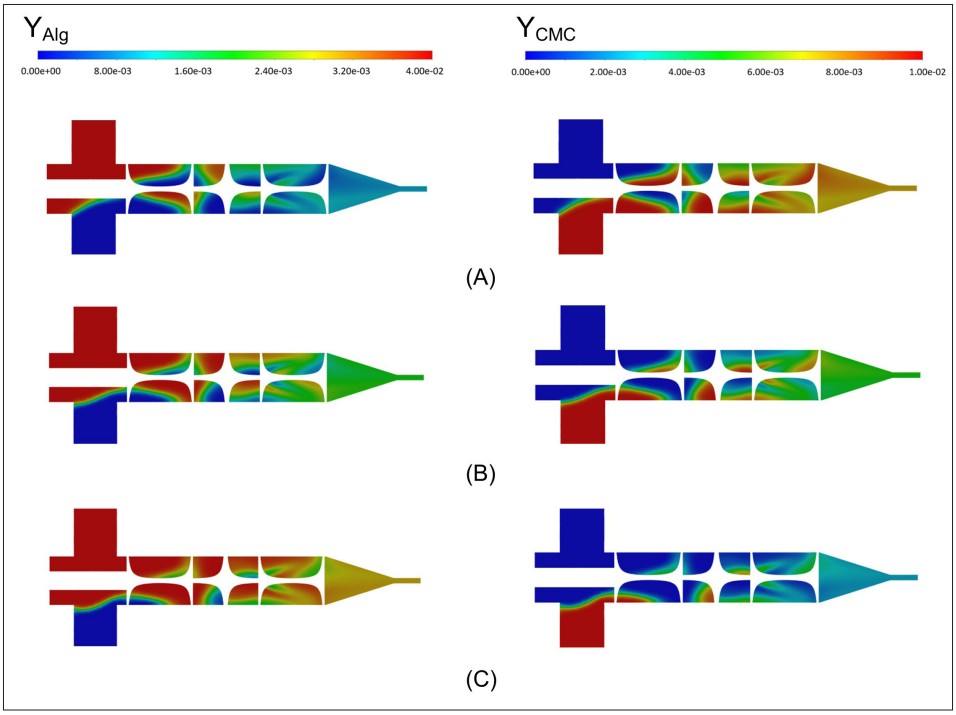

Figure 13. Distribution of mass fractions of (left) alginate and (right) carboxymethylcellulose during multi-material bioprinting for (A) α = 0.5, (B) α = 1, (C) α = 1.5.

time. Since this initial delay is predictable, its effect on composition control can be eliminated by advancing the inlet flow rate changes by t_0. However, the overall transition time for composition change is longer and varies across different mixing scenarios. Figure 16 shows the variation in MI for cases corresponding to Figure 15. The initial delay is clearly visible, followed by a dip in MI, with a minimum occurring 35–50% of the sweep time. This minimum homogeneity point is important for toolpath design, as significant drops in MI (especially below 0.95) may lead to precursor separation and the formation of streaky fibers (Figure 1). For applications requiring high structural integrity, this point should be carefully considered—particularly if it occurs at a scaffold surface, where it may compromise mechanical performance under shear or frictional stress. Following the minimum, MI increases monotonically until it reaches a steady-state value. For the 5mm/s printing speed cases shown in Figures 15 and 16, the initial delay again occurs around 20–25% of the sweep time, and the minimum homogeneity point arises at a similar sweep time fraction as in the 10 mm/s case. However, due to the longer residence time at 5 mm/s, the outflow stream becomes more thoroughly mixed, rendering the minimum homogeneity point less critical. Figures 15B and 16B illustrate changes in ψ and MI for reverse transitions, i.e., from different α values back to α = 1. Compared to Figures 15A and 16A, these represent reciprocal composition changes between high and low alginate or CMC concentrations, which may occur during controlled-gradient multi-material bioprinting. Notably, the initial delay remains consistent across all reverse cases, just as it does in the forward transitions. The minimum homogeneity point also occurs within a similar sweep time range.

The transition time for a composition change can be calculated based on either the MI or the outlet concentration ratio (ψ). However, as shown in Figure 16, most cases—except for the transition from α = 1→0.5 with V = 10 mm/s—remain within the fully mixed region (MI > 0.95), where the MI threshold is insufficient to define transition time. Therefore, transition time was instead calculated based on the outlet concentration ratio ψ, adopting a 5% deviation from the final (target) value as criterion. Figure 17 reports the transition times for various composition changes. The results show that transition times are almost identical for both forward and reverse transitions when $\alpha \geq 1$. However, for $\alpha \leq 1$, transitions toward higher alginate content (i.e., $\alpha \rightarrow 1$) have shorter transition times compared to the reverse direction (i.e., $1 \rightarrow \alpha$).

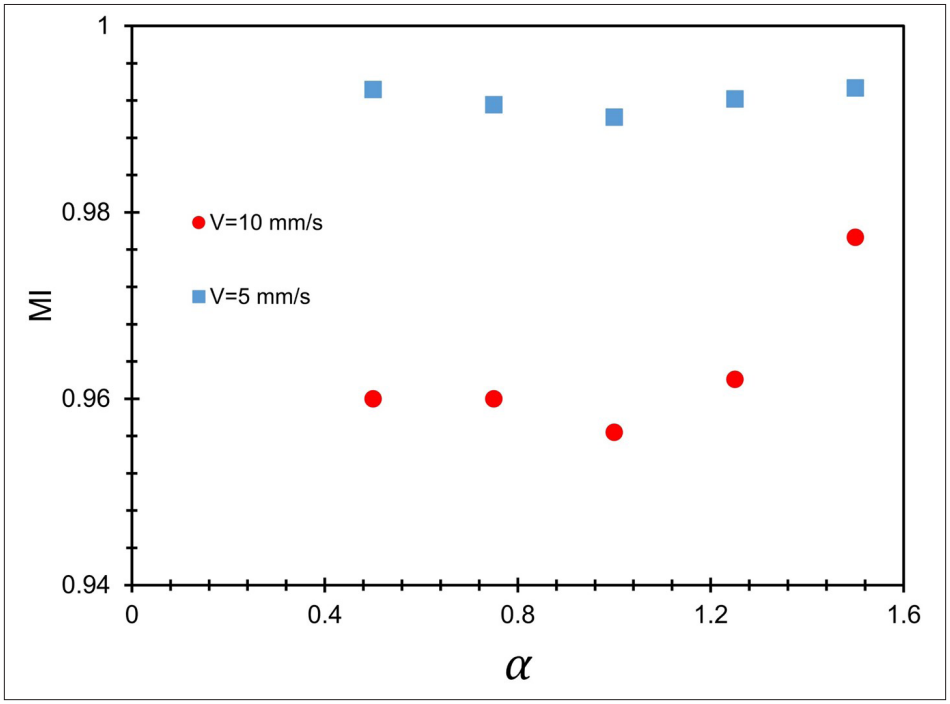

Figure 14. Variation of mixing index (MI) with alginate flow ratio (α) under different printing speeds.

Using a particle tracking method, Regner et al.[74] defined separate residence times for each component of a mixture and showed that, during transient flow, the more viscous precursor exhibits a longer residence time compared to the less viscous one. Moreover, this residence time difference increases with the viscosity ratio of the two precursors. Neglecting surface tension effects and assuming equal shear stress across the interface between the precursor streams, the stream with lower apparent viscosity experiences a higher shear rate, leading to greater stretching and the formation of thinner striations. This enhances mixing within the helical mixer, as previously explained by Jaffer and Wood[73] in the context of Newtonian fluid mixing. For the shear-thinning biomaterials used in the current study, a higher shear rate in the low-viscosity CMC stream further reduces its apparent viscosity, promoting even more stretching on that side of the interface. Additionally, increasing the flow rate of the more viscous precursor (alginate) while maintaining the same total flow rate increases the velocity and shear rate differences at the interface. This leads to finer striations of the lower-viscosity precursor (CMC) and thus better mixing. Since transition time is determined based on reaching the target composition (ψ), improved mixing translates into a shorter transition time.

The effective shear rate for flow inside a helical mixer can be estimated as[43]:

$$\dot{\gamma}_{eff} = \frac{112\ Q}{\pi\ d^3} \qquad \text{(XXXIX)}$$

This effective shear rate is used to calculate the characteristic apparent viscosity of each biomaterial solution (via **Equation XXIX**) and of the mixture (using **Equations XXX–XXXII**) inside the printing head with a helical mixer. Figure 18 presents the apparent viscosity of various alginate–CMC solutions under effective shear rates corresponding to printing speeds of 10 and 5 mm/s. An increase in ψ reflects a higher alginate concentration in the printed fiber and also a higher α value (see **Equation XV**). As shown in Figure 18, higher ψ or α values are associated with alginate–CMC solutions with higher apparent viscosity. Accordingly, the results in Figures 14–17 suggest improved mixing performance for outlet mixtures with higher apparent viscosity. In practical terms, adjusting the toolpath in controlled-gradient multi-material bioprinting to follow a positive viscosity gradient can shorten the transition time. This holds true when increasing the mass fraction of one precursor (i.e., increasing α or β) results in a noticeable increase in the apparent viscosity of the mixture within the effective shear rate range, as shown in Figure 18. However, printing along a positive viscosity gradient may deform lower scaffold layers or cause mechanical failure. Therefore, appropriate

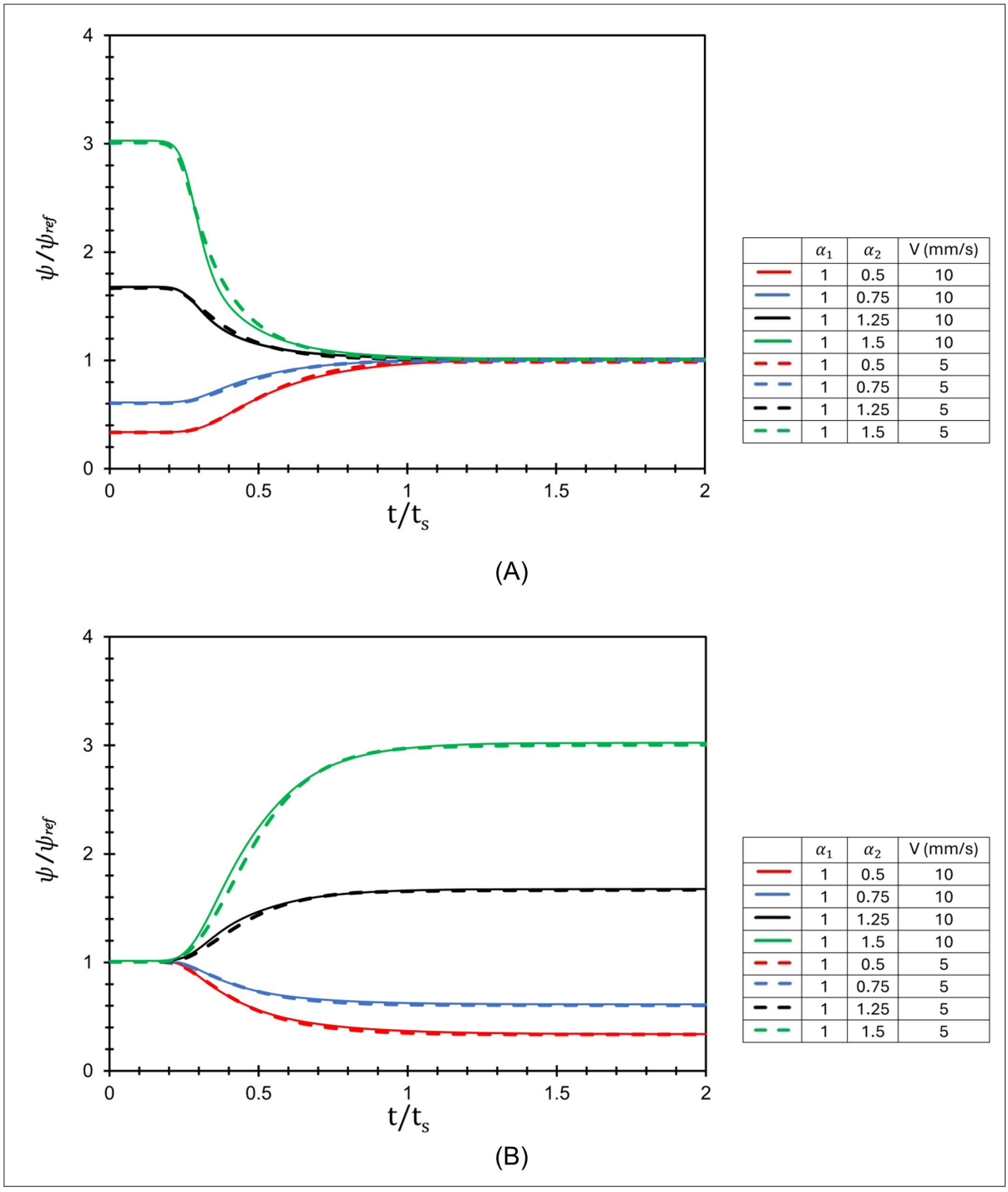

Figure 15. Temporal variation of normalized concentration ratio for various composition changes: (A) $\alpha_1 \rightarrow \alpha_2$, (B) $\alpha_2 \rightarrow \alpha_1$.

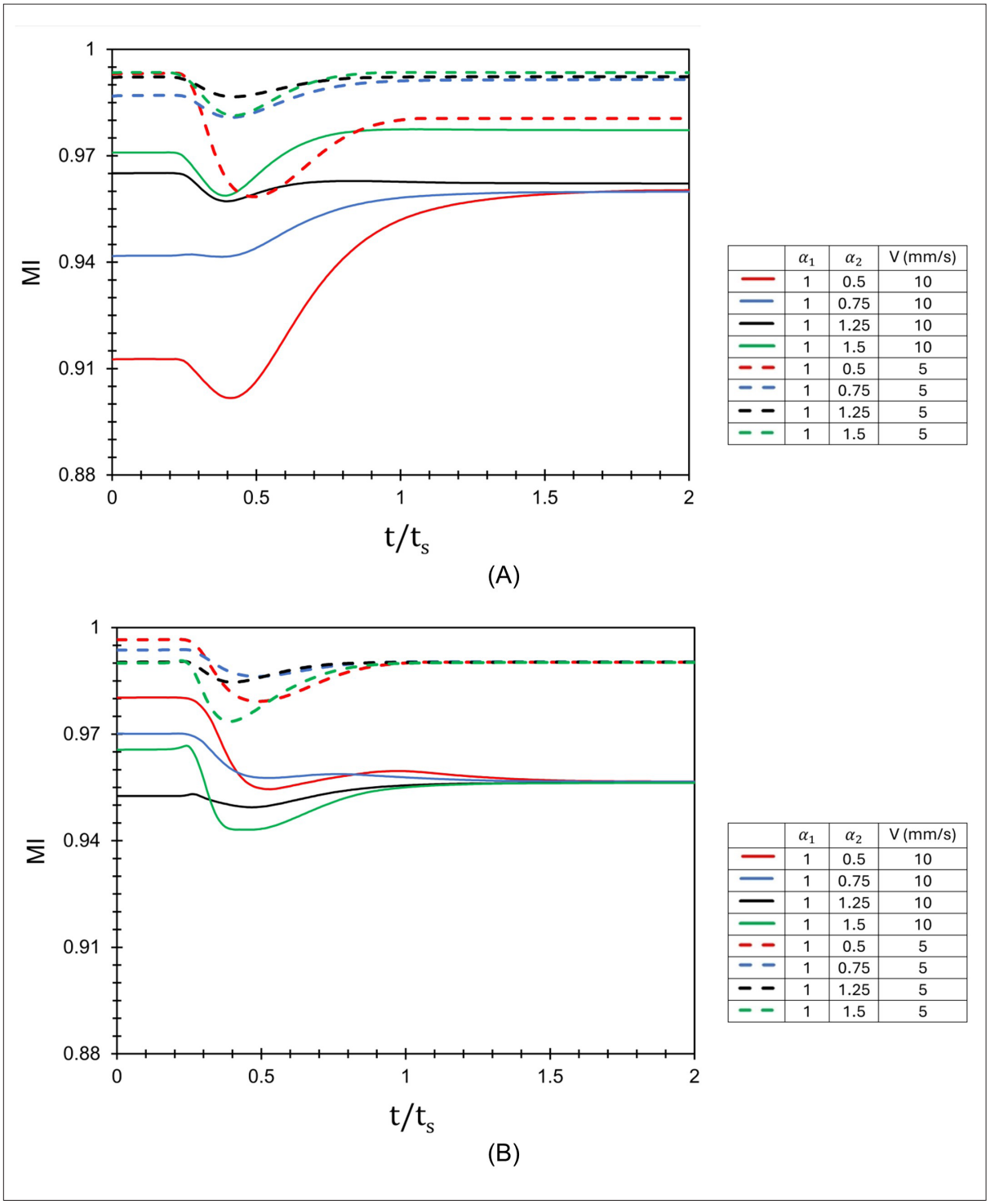

Figure 16. Temporal variation of mixing index (MI) for composition changes: (A) $\alpha_1 \rightarrow \alpha_2$, (B) $\alpha_2 \rightarrow \alpha_1$.

crosslinking of the lower layers is required to maintain the structural integrity of the scaffold.

As an extreme test case, the head was examined for a composition change from α = 0.5 to α = 1.5, and vice versa, representing a significant change in composition (between ψ = 1.33 and ψ = 12). Figure 19A and B illustrates the corresponding outflow stream composition and MI from CFD simulations. The initial delay and minimum homogeneity points are almost identical to those observed in Figures 15 and 16, confirming that these characteristics are independent of the initial and target compositions. The transition times for $\alpha = 0.5 \rightarrow 1.5$ and its reverse case are shown in Figure 17, alongside other scenarios. Comparing these results confirms that transitions toward higher-viscosity compositions result in shorter transition times.

The transition times shown in Figure 17 can be further reduced by advancing the flow rate changes based on the initial delay (t_0). When transition time is multiplied by the printing speed, it yields the transition length, representing the spatial resolution of the printer for printing fibers with composition gradients (neglecting the delay in mechanical and electrical control systems). To highlight the improvement in spatial resolution, Table 6 presents the relative change in spatial resolution (transition length) resulting from advancing the inlet flow rate changes by $t_0 = 0.2t_s$. The table shows a 17–30% improvement in the spatial resolution of the composition gradient. The smallest improvement occurs in the extreme case with a negative viscosity gradient ($\alpha = 1.5 \rightarrow 0.5$), while the largest improvements are observed for moderate composition changes in the $\alpha \geq 1$ range ($\alpha = 1 \leftrightarrows 1.25$).

Comparing the normalized transition time values for various composition changes in Figure 17—and considering the overall insights from the computational results—it can be concluded that adjusting the overall print direction toward a higher fraction of the more viscous precursor can improve the spatial resolution of controlled composition gradient printing. To ensure precise control over fiber composition and to improve the spatial resolution of composition gradients in multi-material bioprinting, the following steps are recommended:

(i) If increasing the mass fraction of one precursor effectively enhances the apparent viscosity of the mixture (calculated based on effective strain rate from **Equation XXXIX**), and if printability considerations (i.e., structural integrity) allow, adjust the printing direction in the toolpath to produce a predominantly positive gradient in apparent viscosity along the fiber.

(ii) Calculate ψ_{ref} using **Equation IX**, based on the mass fractions of the precursors.

(iii) Select a suitable printing speed, then calculate the reference inlet flow rates using **Equations V and VIII**. Calculate the corresponding reference mass

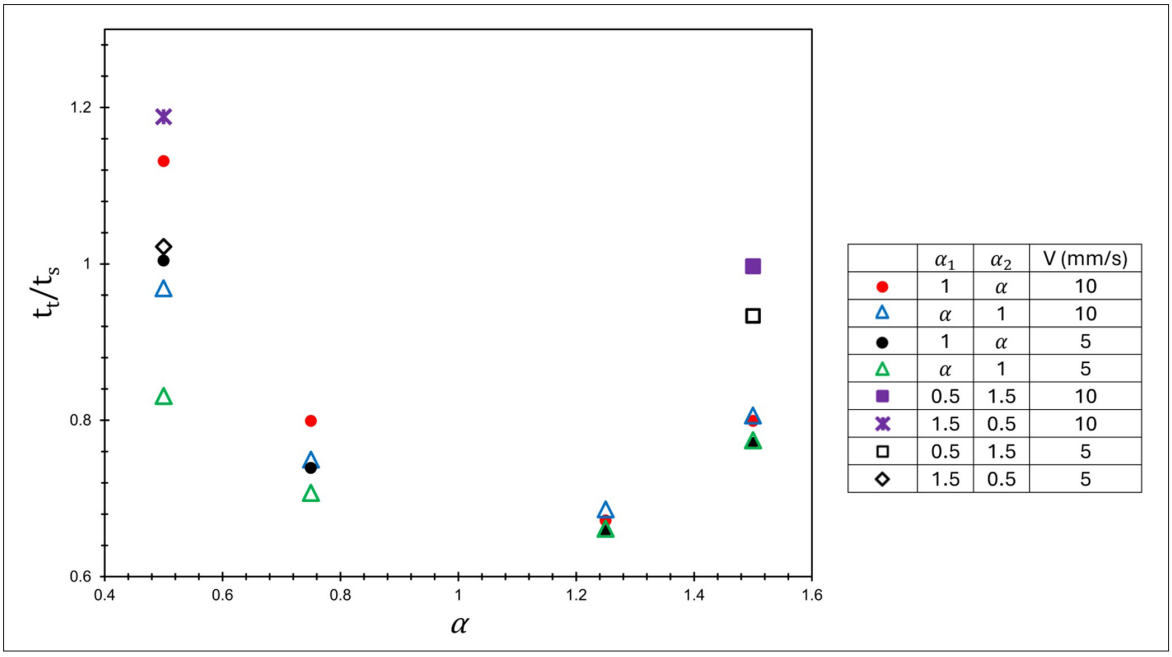

Figure 17. Variation of normalized transition time for different composition changes.

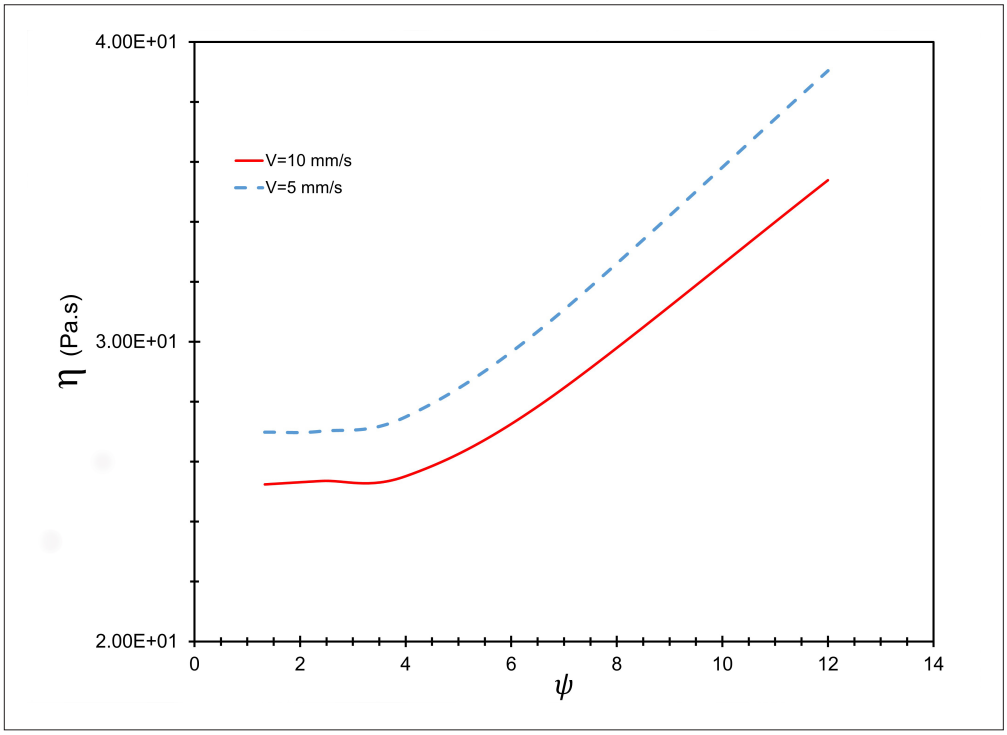

Figure 18. Apparent viscosity of alginate–carboxymethylcellulose solutions with various concentration ratios under effective shear rates corresponding to different printing speeds.

fractions at the outflow stream using **Equations X and XI**.

(iv) If the reference composition, characterized by ψ_{ref}, differs from the intended fiber composition, calculate the required α and β using **Equation XV** to achieve the target concentration ratio (ψ) at the outflow. Then, calculate the corresponding inlet flow rates using **Equations XII and XIII**.

(v) During the printing process, dynamically adjust the fiber composition by updating α and β, which determines the inlet mass flow rates based on **Equations XII and XIII**.

(vi) Advance each change in α and β by the delay time t_0, as predicted by CFD simulations, to improve the spatial resolution of the resulting composition gradient.

For multi-material bioprinting with precursors other than alginate–CMC, the initial delay time may differ from the range identified in this study (0.2–0.25 t_s) and should be determined based on CFD simulations tailored to the specific precursors.

If there is flexibility in selecting the mass fractions at the inlets, using precursor streams with smaller differences in apparent viscosity (calculated at the effective shear rate) can facilitate more efficient mixing in the helical mixer.[74] Additionally, when consecutive changes in fiber composition are required, careful selection of inlet mass fractions can help set a reference point near the midpoint of the overall composition range, thereby preventing large, abrupt changes in composition. For example, if the overall composition range falls ψ = 6–12, selecting a reference point at ψ = 9—the midpoint—can lead to shorter transition delays and better control over the composition gradient within the printed scaffold. This is because the selected reference point results in moderate mass fractions at the inlet (determined using **Equations XII–XV**), which in turn require minimal adjustments to achieve the full range of intended composition change during printing.

The applicability of the analyses presented in this study relies on the prior assumption that all intended compositions are printable under appropriate printing conditions, as established in **Section 2.7**. However, in real-world applications involving diverse biomaterials—many of which exhibit viscoelastic and thixotropic behavior—the stress history during mixing can influence both printability and cell viability,[75,76] potentially resulting in discrepancies between experimental outcomes and the computational simulations and analyses presented in this study.

Table 6. Relative improvement in spatial resolution of the composition gradient when advancing flow rate changes by $t_0 = 0.2t_s$

α_1	α_2	Relative improvement $\left(\frac{\Delta \ell_t}{\ell_t}\right)$			
		V = 10 mm/s		V = 5 mm/s	
		$\alpha_1 \rightarrow \alpha_2$	$\alpha_2 \rightarrow \alpha_1$	$\alpha_1 \rightarrow \alpha_2$	$\alpha_2 \rightarrow \alpha_1$
1	0.5	0.18	0.21	0.20	0.24
1	0.75	0.25	0.27	0.27	0.28
1	1.25	0.30	0.29	0.30	0.30
1	1.5	0.25	0.25	0.26	0.26
0.5	1.5	0.20	0.17	0.21	0.19

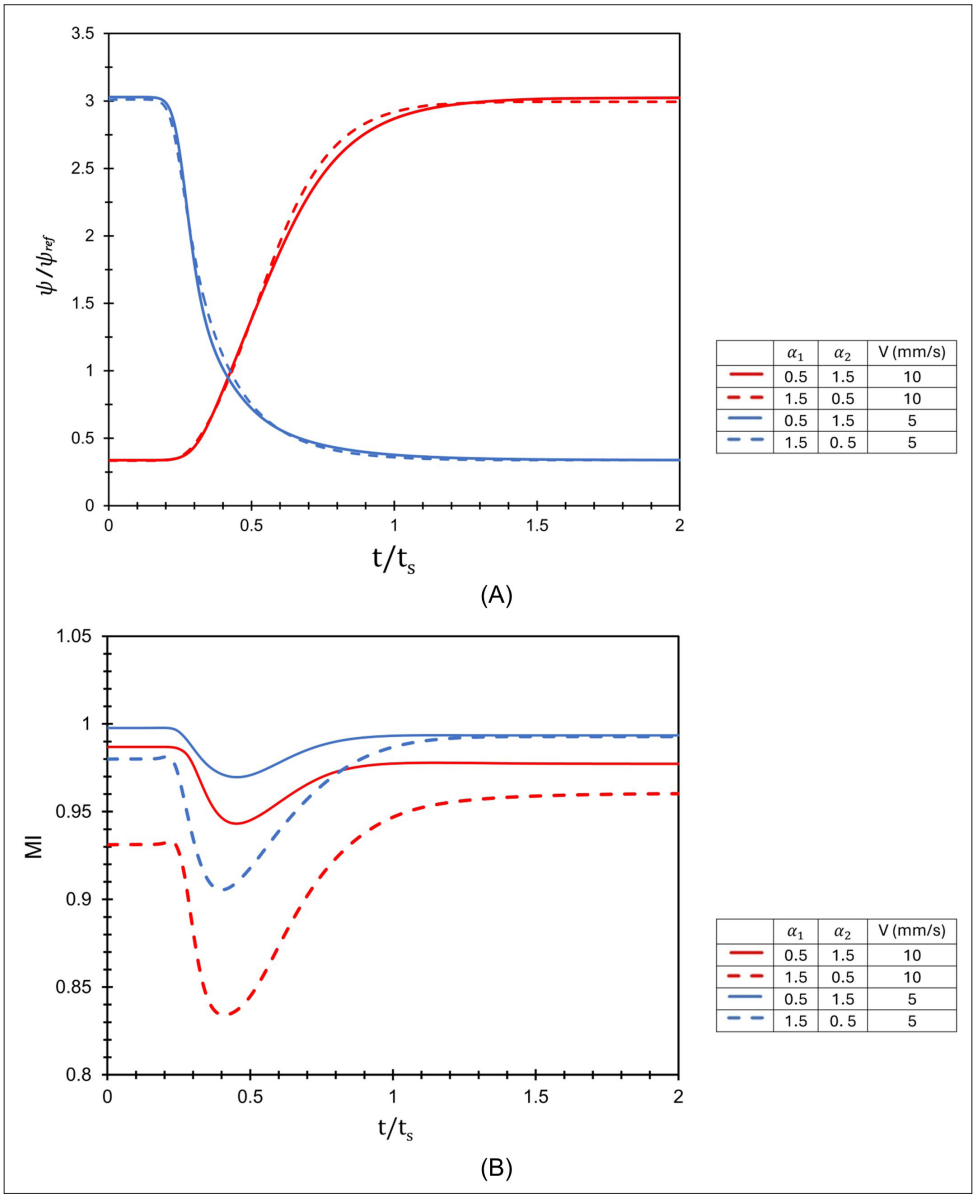

Figure 19. Temporal variation of (A) normalized concentration ratio and (B) mixing index (MI) for extreme composition changes.

Moreover, the computational and mathematical models used in this study do not account for complex cell–biomaterial interactions during mixing within the print head or during the crosslinking process after fiber deposition. Therefore, the performance of the designed multi-material bioprinting head should be experimentally validated. This involves fabricating the designed head, integrating it into a bioprinting system, printing multi-material fibers, and assessing both printability and cell viability in the printed constructs.

4. Conclusion

Multi-material bioprinting with controlled composition gradients is a promising approach for accurately replicating the heterogeneous structures of native tissues in printed constructs. Despite its potential, comprehensive studies on the performance of printing heads equipped with helical static mixers for this application remain limited. This study aimed to address this gap by investigating biomaterial mixing and exploring design modifications and flow control strategies to enhance the spatial resolution of composition gradients. CFD simulations served as the primary tool for this investigation and were validated against experimental data. Based on these validated simulations, a multi-material bioprinting head with a helical mixer was designed. The CFD results revealed the effects of various geometrical parameters on mixing performance, process-induced forces, and internal volume.

A mathematical framework was developed to describe the characteristic parameters governing the outflow conditions during composition changes. While the head geometry was optimized using numerical simulation involving two 4% alginate aqueous solutions, further evaluation using alginate–CMC aqueous mixtures demonstrated the head's capability to print fibers with controlled composition gradients. A composition- and temperature-dependent Cross non-Newtonian viscosity model was fitted to rheological test data of various alginate–CMC aqueous solutions to relate their apparent viscosity to precursor mass fractions across a range of temperatures. Although the numerical simulations of multi-material bioprinting addressed alginate–CMC systems, the insights gained are broadly applicable to the design and operation of multi-material heads for gradient-based bioprinting.

Numerical results for mixing 4% alginate and 1% CMC aqueous solutions demonstrated that the transition time for composition changes includes an initial delay of about 20–25% of the sweep time. A streaky pattern with reduced homogeneity may appear in the printed fiber for 35–50% of the sweep time. Lower printing speeds can mitigate this issue by increasing residence time and promoting more thorough mixing. Based on numerical results covering a wide range of fiber composition changes, an algorithm was developed to improve control over composition gradients in multi-material bioprinting by reducing transition time. Specifically, for bioprinting with 4% alginate and 1% CMC aqueous solutions, combining the modified head geometry with an adjustment of inlet flow rate timing (to account for the initial delay) resulted in a 17–30% improvement in the spatial resolution of composition gradients. Additionally, designing the toolpath to follow a positive gradient in apparent viscosity further improved gradient resolution.

While real-world multi-material bioprinting involves diverse biomaterials with varying properties, CFD simulations offer valuable insights into processes involving controlled composition gradients. In practical applications, CFD can predict outcomes such as MIs, transition times, and flow dynamics, guiding adjustments to enhance spatial resolution along the fiber. However, the actual performance of the bioprinting head should be validated experimentally. This requires fabricating the prototype, integrating it into a bioprinting system, and assessing both printability and cell viability in the printed constructs.

Acknowledgments

The authors extend their appreciation to the GESIM company for sharing the technical datasheets of the GESIM Bioscaffolder.

Funding

This work was supported by the University of Saskatchewan Dean's Scholarship and the Devolved Scholarship from the Department of Mechanical Engineering for the first author, and by the Natural Sciences and Engineering Research Council (NSERC) funds (Grant numbers: RGPIN 06396-2019, RGPIN 04981-2022) for the co-authors.

Conflict of interest

Xiongbiao Chen serves as the Editorial Board Member of the journal, but did not in any way involve in the editorial and peer-review process conducted for this paper, directly or indirectly. Other authors declare they have no competing interests.

Author contributions

Conceptualization: All authors
Formal analysis: Reza Gharraei
Funding acquisition: Xiongbiao Chen, Donald J. Bergstrom

Investigation: Reza Gharraei
Methodology: Reza Gharraei
Validation: Reza Gharraei
Supervision: Xiongbiao Chen, Donald J. Bergstrom
Writing–original draft: Reza Gharraei
Writing–review & editing: All authors

Ethics approval and consent to participate

Not applicable.

Consent for publication

Not applicable.

Availability of data

Data is available from the corresponding author upon reasonable request.

References

1. Ozbolat IT, Moncal KK, Gudapati H. Evaluation of bioprinter technologies. *Addit Manuf*. 2017;13:179-200. doi: 10.1016/j.addma.2016.10.003
2. Levato R, Jungst T, Scheuring RG, Blunk T, Groll J, Malda J. From shape to function: the next step in bioprinting. *Adv Mater*. 2020;32(12):1906423. doi: 10.1002/adma.201906423
3. Rutz AL, Hyland KE, Jakus AE, Burghardt WR, Shah RN. A multimaterial bioink method for 3D printing tunable, cell-compatible hydrogels. *Adv Mater*. 2015;27(9):1607-1614. doi: 10.1002/adma.201405076
4. Chen XB, Fazel Anvari-Yazdi A, Duan X, et al. Biomaterials/bioinks and extrusion bioprinting. *Bioact Mater*. 2023;28:511-536. doi: 10.1016/j.bioactmat.2023.06.006
5. Sodupe-Ortega E, Sanz-Garcia A, Pernia-Espinoza A, Escobedo-Lucea C. Accurate calibration in multi-material 3D bioprinting for tissue engineering. *Materials*. 2018;11(8):1402. doi: 10.3390/ma11081402
6. Betancourt N, Chen X. Review of extrusion-based multi-material bioprinting processes. *Bioprinting*. 2022;25:e00189. doi: 10.1016/j.bprint.2021.e00189
7. Wei Q, Zhou J, An Y, Li M, Zhang J, Yang S. Modification, 3D printing process and application of sodium alginate based hydrogels in soft tissue engineering: a review. *Int J Biol Macromol*. 2023;232:123450. doi: 10.1016/j.ijbiomac.2023.123450
8. Kang HW, Lee SJ, Ko IK, Kengla C, Yoo JJ, Atala A. A 3D bioprinting system to produce human-scale tissue constructs with structural integrity. *Nat Biotechnol*. 2016;34(3):312-319. doi: 10.1038/nbt.3413
9. Ozbolat IT, Hospodiuk M. Current advances and future perspectives in extrusion-based bioprinting. *Biomaterials*. 2016;76:321-343. doi: 10.1016/j.biomaterials.2015.10.076
10. Liu W, Zhang YS, Heinrich MA, et al. Rapid continuous multimaterial extrusion bioprinting. *Adv Mater*. 2017;29(3):1604630. doi: 10.1002/adma.201604630
11. Wei Q, An Y, Zhao X, Li M, Zhang J. Three-dimensional bioprinting of tissue-engineered skin: Biomaterials, fabrication techniques, challenging difficulties, and future directions: a review. *Int J Biol Macromol*. 2024;266(1):131281. doi: 10.1016/j.ijbiomac.2024.131281
12. Tirella A, De Maria C, Criscenti G, Vozzi G, Ahluwalia A. The PAM 2 system: a multilevel approach for fabrication of complex three-dimensional microstructures. *Rapid Prototyp J*. 2012;18(4): 299-307. doi: 10.1108/13552541211231725
13. Ning L, Sun H, Lelong T, et al. 3D bioprinting of scaffolds with living Schwann cells for potential nerve tissue engineering applications. *Biofabrication*. 2018;10(3): 035014. doi: 10.1088/1758-5090/aacd30
14. Sarker Md, Izadifar M, Schreyer D, Chen X. Influence of ionic crosslinkers (Ca^{2+} /Ba^{2+} /Zn^{2+}) on the mechanical and biological properties of 3D bioplotted hydrogel scaffolds. *J Biomater Sci Polym Ed*. 2018;29(10):1126-1154. doi: 10.1080/09205063.2018.1433420
15. Naghieh S, Karamooz-Ravari MR, Sarker M, Karki E, Chen X. Influence of crosslinking on the mechanical behavior of 3D printed alginate scaffolds: experimental and numerical approaches. *J Mech Behav Biomed Mater*. 2018;80:111-118. doi: 10.1016/j.jmbbm.2018.01.034
16. Izadifar Z, Chang T, Kulyk W, Chen X, Eames BF. Analyzing biological performance of 3D-printed, cell-impregnated hybrid constructs for cartilage tissue engineering. *Tissue Eng Part C Methods*. 2016;22(3):173-188. doi: 10.1089/ten.tec.2015.0307
17. Cameron T, Naseri E, MacCallum B, Ahmadi A. Development of a disposable single-nozzle printhead for 3D bioprinting of continuous multi-material constructs. *Micromachines (Basel)*. 2020;11(5):459. doi: 10.3390/MI11050459
18. Snyder J, Son AR, Hamid Q, Wu H, Sun W. Hetero-cellular prototyping by synchronized multi-material bioprinting for rotary cell culture system. *Biofabrication*. 2016;8(1):015002. doi: 10.1088/1758-5090/8/1/015002
19. Ashammakhi N, Ahadian S, Xu C, et al. Bioinks and bioprinting technologies to make heterogeneous and biomimetic tissue constructs. *Mater Today Bio*. 2019;1:100008. doi: 10.1016/j.mtbio.2019.100008

20. Colosi C, Shin SR, Manoharan V, et al. Microfluidic bioprinting of heterogeneous 3D tissue constructs using low-viscosity bioink. *Adv Mater*. 2016;28(4):677-684. doi: 10.1002/adma.201503310

21. du Chatinier DN, Figler KP, Agrawal P, Liu W, Zhang YS. The potential of microfluidics-enhanced extrusion bioprinting. *Biomicrofluidics*. 2021;15(4):041304. doi: 10.1063/5.0033280

22. Blaeser A, Duarte Campos DF, Puster U, Richtering W, Stevens MM, Fischer H. Controlling shear stress in 3D bioprinting is a key factor to balance printing resolution and stem cell integrity. *Adv Healthc Mater*. 2016;5(3):326-333. doi: 10.1002/adhm.201500677

23. Alloca PT. Mixing efficiency of static mixing units in laminar flow. *Fiber Prod*. 1982;10(1):12-19.

24. Heywood NI, Viney LJ, Stewart IW. Mixing efficiencies and energy requirements of various motionless mixer designs for laminar mixing applications. In: *Institution of Chemical Engineers Symposium Series*. 1984;89:147-176. doi: 10.1016/b978-0-85295-171-2.50013-x

25. Ober TJ, Foresti D, Lewis JA. Active mixing of complex fluids at the microscale. *Proceedings of the National Academy of Sciences of the United States of America*. 2015;112(40):12293-12298. doi: 10.1073/pnas.1509224112

26. Chávez-Madero C, de León-Derby MD, Samandari M, et al. Using chaotic advection for facile high-throughput fabrication of ordered multilayer micro- and nanostructures: continuous chaotic printing. *Biofabrication*. 2020;12(3):035023. doi: 10.1088/1758-5090/ab84cc

27. Puertas-Bartolomé M, Włodarczyk-Biegun MK, del Campo A, Vázquez-Lasa B, San Román J. 3D printing of a reactive hydrogel bio-ink using a static mixing tool. *Polymers (Basel)*. 2020;12(9):1986. doi: 10.3390/polym12091986

28. Giachini PAGS, Gupta SS, Wang W, et al. Additive manufacturing of cellulose-based materials with continuous, multidirectional stiffness gradients. *Sci Adv*. 2020;6(8):eaay0929. doi: 10.1126/sciadv.aay0929

29. Kuzucu M, Vera G, Beaumont M, et al. Extrusion-based 3D bioprinting of gradients of stiffness, cell density, and immobilized peptide using thermogelling hydrogels. *ACS Biomater Sci Eng*. 2021;7(6):2192-2197. doi: 10.1021/acsbiomaterials.1c00183

30. Chand R, Muhire BS, Vijayavenkataraman S. Computational fluid dynamics assessment of the effect of bioprinting parameters in extrusion bioprinting. *Int J Bioprint*. 2022;8(2):545. doi: 10.18063/ijb.v8i2.545

31. Lee S, Son M, Lee J, et al. Computational fluid dynamics analysis and empirical evaluation of carboxymethylcellulose/alginate 3D bioprinting inks for screw-based microextrusion. *Polymers (Basel)*. 2024;16(8):1137. doi: 10.3390/polym16081137

32. Fareez UNM, Naqvi SAA, Mahmud M, Temirel M. Computational fluid dynamics (CFD) analysis of bioprinting. *Adv Healthc Mater*. 2024;13(20):2400643. doi: 10.1002/adhm.202400643

33. Martanto W, Baisch SM, Costner EA, Prausnitz MR, Smith MK. Fluid dynamics in conically tapered microneedles. *AIChE J*. 2005;51(6):1599-1607. doi: 10.1002/aic.10424

34. Liravi F, Darleux R, Toyserkani E. Additive manufacturing of 3D structures with non-Newtonian highly viscous fluids: finite element modeling and experimental validation. *Addit Manuf*. 2017;13:113-123. doi: 10.1016/j.addma.2016.10.008

35. Li Y, Liu Y, Jiang C, Li S, Liang G, Hu Q. A reactor-like spinneret used in 3D printing alginate hollow fiber: a numerical study of morphological evolution. *Soft Matter*. 2016;12(8):2392-2399. doi: 10.1039/c5sm02733k

36. Li S, Liu Y, Li Y, Zhang Y, Hu Q. Computational and experimental investigations of the mechanisms used by coaxial fluids to fabricate hollow hydrogel fibers. *Chem Eng Process Process Intensif*. 2015;95:98-104. doi: 10.1016/j.cep.2015.05.018

37. Samandari M, Alipanah F, Majidzadeh-A K, Alvarez MM, Trujillo-de Santiago G, Tamayol A. Controlling cellular organization in bioprinting through designed 3D microcompartmentalization. *Appl Phys Rev*. 2021;8(2):021404. doi: 10.1063/5.0040732

38. Ceballos-González CF, Bolívar-Monsalve EJ, Quevedo-Moreno DA, et al. Plug-and-play multimaterial chaotic printing/bioprinting to produce radial and axial micropatterns in hydrogel filaments. *Adv Mater Technol*. 2023;8(17):2202208. doi: 10.1002/admt.202202208

39. Ates G, Bartolo P. Computational fluid dynamics for the optimization of internal bioprinting parameters and mixing conditions. *Int J Bioprint*. 2023;9(6):0219. doi: 10.36922/ijb.0219

40. Wei Q, An Y, Zhao X, Li M, Zhang J, Cui N. Optimal design of multi-biomaterials mixed extrusion nozzle for 3D bioprinting considering cell activity. *Virtual Phys Prototyp*. 2025;20(1):e2438897. doi: 10.1080/17452759.2024.2438897

41. *Series 190 disposable plastic spiral bayonet mixer.* v111424, Nordson-EFD, 2024:2.

42. Chen DXB. *Extrusion Bioprinting of Scaffolds for Tissue Engineering Applications*. 1st ed. Springer Nature; 2019. doi: 10.1007/978-3-030-03460-3

43. Paul EL, Atiemo-Obeng VA, Kresta SM, eds. *Handbook of Industrial Mixing*. New Jersey, NJ: John Wiley & Sons; 2003. doi: 10.1002/0471451452
doi: 10.1002/0471451452

44. Chahabra RP, Richardson JF. *Non-Newtonian Flow and Applied Rheology, Engineering Applications*. 2nd ed. Oxford, UK: Butterworth-Heinemann; 2008. doi: 10.1016/B978-0-7506-8532-0.X0001-7

45. White FM. *Viscous Fluid Flow*. Boston, MA, Mcgraw Hill; 2006.

46. Ribeiro ACF, Fabela I, Sobral AJFN, et al. Diffusion of sodium alginate in aqueous solutions at T=298.15K. *J Chem Thermodyn*. 2014;74:263-268. doi: 10.1016/j.jct.2014.02.014

47. Paradies HH, Wagner D, Fischer WR. Multicomponent diffusion of sodium alginate solutions with added salt. II. Charged vs. uncharged system. *Berichte der Bunsengesellschaft für physikalische Chemie*. 1996;100(8):1299-1307. doi: 10.1002/bbpc.19961000806

48. Shah NF, Kale DD. Pressure drop for laminar flow of non-Newtonian fluids in static mixers. *Chem Eng Sci*. 1991;46(8):2159-2161. doi: 10.1016/0009-2509(91)80175-X

49. Cybulski, A. and Werner K. Static mixers—criteria for applications and selection. *Int J Chem Eng*. 1986;26:171-180.

50. Grace HP. Dispersion phenomena in high viscosity immiscible fluid systems and application of static mixers as dispersion devices in such systems. *Chem Eng Commun*. 1982;14(3-6):225-277. doi: 10.1080/00986448208911047

51. Wilkinson WL, Cliff MJ. An investigation into the performance of a static inline-mixer. In: *Second European Conference on Mixing*. 1977:A2.15-A2.29.

52. Xu G, Feng L, Li Y, Wang K. Pressure drop of pseudo-plastic fluids in static mixers. *Chin J Chem Eng*. 1997;5:93-96.

53. Nyande BW, Thomas MK, Lakerveld R. CFD analysis of a kenics static mixer with a low pressure drop under laminar flow conditions. *Ind Eng Chem Res*. 2021;60(14):5264-5277. doi: 10.1021/acs.iecr.1c00135

54. White F. *Fluid Mechanics*. 9th ed. New York, NY: Mc GrawHill; 2021.

55. Feng X, Ren Y, Hou L, et al. Tri-fluid mixing in a microchannel for nanoparticle synthesis. *Lab Chip*. 2019;19(17):2936-2946. doi: 10.1039/C9LC00425D

56. Viktorov V, Mahmud MR, Visconte C. Numerical study of fluid mixing at different inlet flow-rate ratios in tear-drop and chain micromixers compared to a new H-C passive micromixer. *Eng Appl Comput Fluid Mech*. 2016;10(1):182-192. doi: 10.1080/19942060.2016.1140075

57. 3D content central, Nordson-EFD. https://www.3dcontentcentral.com/parts/supplier/EFD,-Inc.aspx, access July 24,2025.

58. Jiang X, Yang N, Wang R. Effect of aspect ratio on the mixing performance in the kenics static mixer. *Processes*. 2021;9(3):464. doi: 10.3390/pr9030464

59. Fatima U, Shakaib M, Memon I. Analysis of mass transfer performance of micromixer device with varying confluence angle using CFD. *Chem Pap*. 2020;74(4):1267-1279. doi: 10.1007/s11696-019-00975-8

60. Kim MS, Park SJ, Gu BK, Kim CH. Ionically crosslinked alginate–carboxymethyl cellulose beads for the delivery of protein therapeutics. *Appl Surf Sci*. 2012;262:28-33. doi: 10.1016/j.apsusc.2012.01.010

61. Agarwal T, Narayana SNGH, Pal K, Pramanik K, Giri S, Banerjee I. Calcium alginate-carboxymethyl cellulose beads for colon-targeted drug delivery. *Int J Biol Macromol*. 2015;75:409-417. doi: 10.1016/j.ijbiomac.2014.12.052

62. Habib A, Sathish V, Mallik S, Khoda B. 3D printability of alginate-carboxymethyl cellulose hydrogel. *Materials*. 2018;11(3):454. doi: 10.3390/ma11030454

63. Garrett Q, Simmons PA, Xu S, et al. Carboxymethylcellulose binds to human corneal epithelial cells and is a modulator of corneal epithelial wound healing. *Invest Opthalmol Vis Sci*. 2007;48(4):1559. doi: 10.1167/iovs.06-0848

64. Benchabane A, Bekkour K. Rheological properties of carboxymethyl cellulose (CMC) solutions. *Colloid Polym Sci*. 2008;286(10):1173-1180. doi: 10.1007/s00396-008-1882-2

65. Ma J, Lin Y, Chen X, Zhao B, Zhang J. Flow behavior, thixotropy and dynamical viscoelasticity of sodium alginate aqueous solutions. *Food Hydrocoll*. 2014; 38:119-128. doi: 10.1016/j.foodhyd.2013.11.016

66. Cross MM. Rheology of non-Newtonian fluids: a new flow equation for pseudoplastic systems. *J Colloid Sci*. 1965;20(5):417-437. doi: 10.1016/0095-8522(65)90022-X

67. Messaâdi A, Dhouibi N, Hamda H, et al. A new equation relating the viscosity arrhenius temperature and the activation energy for some newtonian classical solvents. *J Chem*. 2015;2015:1-12. doi: 10.1155/2015/163262

68. Toth G, Nagy D, Bata A, Belina K. Determination of polymer melts flow-activation energy a function of wide range shear rate. *J Phys Conf Ser*. 2018;1045:012040. doi: 10.1088/1742-6596/1045/1/012040

69. Moffat RJ. Describing the uncertainties in experimental results. *Exp Therm Fluid Sci*. 1988;1(1):3-17.
doi: 10.1016/0894-1777(88)90043-X

70. Nair K, Gandhi M, Khalil S, et al. Characterization of cell viability during bioprinting processes. *Biotechnol J*. 2009;4(8):1168-1177.
doi: 10.1002/biot.200900004

71. Ning L, Betancourt N, Schreyer DJ, Chen X. Characterization of cell damage and proliferative ability during and after bioprinting. *ACS Biomater Sci Eng*. 2018;4(11): 3906-3918.
doi: 10.1021/acsbiomaterials.8b00714

72. Miri AK, Mirzaee I, Hassan S, et al. Effective bioprinting resolution in tissue model fabrication. *Lab Chip*. 2019;19(11):2019-2037.
doi: 10.1039/C8LC01037D

73. Jaffer SA, Wood PE. Quantification of laminar mixing in the kenics static mixer: An experimental study. *Can J Chem Eng*. 1998;76(3):516-521.
doi: 10.1002/cjce.5450760323

74. Regner M, Östergren K, Trägårdh C. Influence of viscosity ratio on the mixing process in a static mixer: numerical study. *Ind Eng Chem Res*. 2008;47(9):3030-3036.
doi: 10.1021/ie0708071

75. Cui R, Li S, Li T, et al. Natural polymer derived hydrogel bioink with enhanced thixotropy improves printability and cellular preservation in 3D bioprinting. *J Mater Chem B*. 2023;11(17):3907-3918.
doi: 10.1039/D2TB02786K

76. Maillard M, Fournier S, García-Tuñón E, Courtial EJ. Advances and obstacles to unify the concept of "printability" in ceramics direct ink writing. *Open Ceram*. 2025;23:100808.
doi: 10.1016/j.oceram.2025.100808

APPENDIX

Appendix A

Derivation of the equations describing the dependencies between inlet and outlet flow conditions

Mass conservation:

$$\dot{m}_{out} = \dot{m}_A + \dot{m}_B \tag{A-I}$$

Assuming the inlet streams as aqueous solutions of biomaterials C_1 and C_2, with mass fractions $Y_{C1,A}$ and $Y_{C2,B}$ at the inlets A and B, respectively:

$$\dot{m}_A = \dot{m}_{C1,A} + \dot{m}_{w,A} = Y_{C1,A}\ m_A + Y_{w,A}\ \dot{m}_A \tag{A-II}$$

and

$$\dot{m}_B = \dot{m}_{C2,B} + \dot{m}_{w,B} = Y_{C2,B}\ \dot{m}_B + Y_{w,B}\ \dot{m}_B \tag{A-III}$$

where $Y_{w,A}$, $Y_{w,B}$ are mass fractions of water for inlet streams at A and B, respectively. The compositions of inlet streams remain consistent during the printing task.

Substituting **Equations A-II and A-III** in **Equation A-I**:

$$\dot{m}_{out} = \dot{m}_{C1,A} + \dot{m}_{C2,B} + \dot{m}_{w,A} + \dot{m}_{w,B} \tag{A-IV}$$

For steady operation, as components C_1 and C_2 are feeding solely from inlet A and inlet B, respectively:

$$\begin{aligned} &\dot{m}_{C1,out} = \dot{m}_{C1,A};\ \dot{m}_{C2,out} = \dot{m}_{C2,B};\\ &\dot{m}_{w,out} = \dot{m}_{w,A} + \dot{m}_{w,B} \end{aligned} \tag{A-V}$$

By substitution in **Equation A-IV** and rearranging:

$$Y_{C1,out} + Y_{C2,out} = \frac{\dot{m}_A}{\dot{m}_A + \dot{m}_B} Y_{C1,A} + \frac{\dot{m}_B}{\dot{m}_A + \dot{m}_B} Y_{C2,B} \tag{A-VI}$$

The concentration ratio of precursors at the outlet (ψ) is defined as:

$$\psi = \frac{Y_{C1,out}}{Y_{C2,out}} \tag{A-VII}$$

Reference condition:

$$\dot{m}_{A,ref} = \dot{m}_{B,ref} = \frac{\dot{m}_{out}}{2} \tag{A-VIII}$$

Regarding **Equations A-V and A-VIII**, for the reference case:

$$\psi_{ref} = \frac{Y_{C1,A}}{Y_{C2,B}} \tag{A-IX}$$

Substituting **Equations A-VIII and A-IX** in **Equation A-VI** for the reference case and rearranging:

$$Y_{C1,out,ref} = \frac{\psi_{ref}}{2\left(\psi_{ref}+1\right)}\left(Y_{C1,A} + Y_{C2,B}\right) \tag{A-X}$$

$$Y_{C2,out,ref} = \frac{1}{2\left(\psi_{ref}+1\right)}\left(Y_{C1,A} + Y_{C2,B}\right) \tag{A-XI}$$

Defining flow ratios of precursors, α and β:

$$\alpha = \frac{Y_{C1,out}}{Y_{C1,out,ref}} = \frac{\dot{m}_{C1,out}}{\dot{m}_{C1,out,ref}} = \frac{\dot{m}_A}{\dot{m}_{A,ref}} \tag{A-XII}$$

$$\beta = \frac{Y_{C2,out}}{Y_{C2,out,ref}} = \frac{\dot{m}_{C2,out}}{\dot{m}_{C2,out,ref}} = \frac{\dot{m}_B}{\dot{m}_{B,ref}} \tag{A-XIII}$$

From **Equations A-12, A-13, and A-1**:

$$\frac{\alpha \dot{m}_{A,ref}}{\dot{m}_{out}} + \frac{\beta \dot{m}_{B,ref}}{\dot{m}_{out}} = 1 \tag{A-XIV}$$

Substituting from **Equation A-VIII** leads to:

$$\alpha + \beta = 2 \tag{A-XV}$$

Using **Equations A-VII and A-IX**:

$$\frac{Y_{C1,out}}{Y_{C1,out,ref}} + \frac{\psi_{ref}}{\psi}\frac{Y_{C1,out}}{Y_{C1,out,ref}} = 2 \tag{A-XVI}$$

or

$$\alpha = \frac{2\psi}{\psi + \psi_{ref}},\ \beta = \frac{2\psi_{ref}}{\psi + \psi_{ref}} \tag{A-XVII}$$

Appendix B

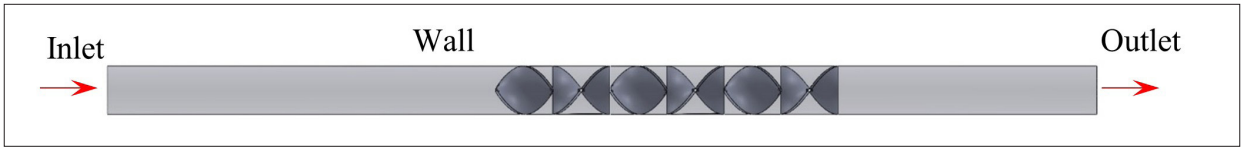

Figure B1. The geometry of the fluid domain for simulation of flow and mixing through a helical mixer inside a pipe (the mixer volume is extracted).